Diagnosing Convection with Weak Temperature Gradient Simulations of DYNAMO

Stipo Sentić[1], Sharon L. Sessions[1], and Željka Fuchs[1,2]

Corresponding author: S. Sentić, Physics Department and Geophysical Research Center, New Mexico Institute of Mining and Technology, 801 Leroy Place, Socorro, NM 87801, USA. (ssentic@nmt.edu)

[1]Physics Department and Geophysical Research Center, New Mexico Institute of Mining and Technology, 801 Leroy Place, Socorro, NM 87801, USA.

[2]Department of Physics, Faculty of Science, Teslina 12, 21000 Split, Croatia.

Abstract.

Determining relationships between convective and environmental diagnostics can improve our understanding of mechanisms controlling tropical convection, and consequently, result in better representations of convection in coarsely resolved models. We identify important diagnostic relationships in observations taken during the Dynamics of the Madden-Julian Oscillation (MJO) campaign, and perform weak temperature gradient (WTG) simulations of DYNAMO convection to determine if the observed relationships are reproduced in our model.

We find that the WTG approximation models local changes in the diagnostics used in the study–precipitation rate, atmospheric stability, moisture, and gross moist stability (GMS)–and reproduces diagnostic relationships suggested in previous studies; an increase in precipitation rate is correlated with increased atmospheric moisture content, which, in turn, is correlated with greater atmospheric stability. Large scale atmospheric stability–changes of which might be related to balanced dynamics, we speculate–seems to be a candidate for a convective controlling mechanism.

Observed and modeled interactions of local convection with the large scale environment–quantified by the GMS–are in agreement with the theory of Inoue and Back (2015b); the GMS increases from small, positive or negative, values during developing convection, and further increases for decaying convection past a characteristic GMS found at peak precipitation rates, atmospheric stability, and moisture content. Understanding the link between the

characteristic GMS and the diagnostics–still a standing problem–could further our understanding of interactions between local convection and the large scale environment.

Three key point statements:

Relationships between convective diagnostics characterize DYNAMO convection.

WTG simulations reproduce observed diagnostic relationships.

GMS characterizes convective development and decay.

1. Introduction

The Madden Julian Oscillation [MJO, *Madden and Julian*, 1972] ties weather and climate [*Zhang*, 2013]: it regulates meteorology from the shortest time scales (precipitation, tornadoes, floods, fires, lightning, tropical cyclones) to the longest time scales (surface temperatures, extratropical climate modes, ENSO, Indian ocean dipole). Current weather and climate prediction models do not capture the MJO adequately [*Kim et al.*, 2014; *Benedict et al.*, 2014], in part because convective parameterizations are not properly modeling relationships between convection and the large scale environment in which it is embedded. In order to improve our ability to model the MJO, and consequently the climate, we need to improve convective parameterizations. One way to to do this is is to improve our understanding of the relationships between convective processes and large scale conditions.

Quantitative relationships between convective parameters and large scale environmental conditions are a standing problem in modeling convection. For example, there is no consensus on the quantitative relationship between precipitation rate and moisture. Studies using satellite observations [*Back and Bretherton*, 2006; *Peters and Neelin*, 2006; *Masunaga*, 2012] and combined observation-numerical modeling studies [*Raymond et al.*, 2007] have proposed several forms of the precipitation rate–moisture relationship in the tropics; though they differ in detail, they all suggest that precipitation is a sensitive function of moisture. Studies have shown that general circulation models improve when precipitation rate depends on moisture quantity [*Sherwood et al.*, 2010]. Further, both idealized numerical studies [*Sessions et al.*, 2010, 2015] and numerical case studies [*Wang*

et al., 2014] find that there is a relationship between the precipitation rate and the import or export of large scale energy and moisture. Obtaining better diagnostic relationships between precipitation rate, moisture, and energy transport on the large scale–in the context of tropical convection–can improve parameterizations relevant to climate and weather predictions.

To understand how tropical convection interacts with the large scale environment, we model convection by parameterizing the large scale. One approach is to impose a mean, time dependent, vertical velocity profile that is consistent with large scale conditions in a model domain [*Fridlind et al.*, 2012; *Woolnough et al.*, 2010; *Wang et al.*, 2014] supplemented by horizontal temperature and moisture tendencies. This approach constrains the convection in a manner that reproduces the observed precipitation very closely. Problems, however, can arise in interpretation of results because imposing vertical motion constrains the precipitation and obscures causal mechanisms. More recent approaches do not specify the vertical motion but utilize an alternate parameterization of the large scale. Two examples are the weak temperature gradient [WTG, *Sobel and Bretherton*, 2000; *Raymond and Zeng*, 2005] and the weak pressure gradient [WPG, *Kuang*, 2008; *Romps*, 2012a, b] approximations. From these approximations the vertical velocity is calculated from convection responding to observed large scale conditions. The advantage of the WTG and WPG approximations is that the model convection is free to evolve, and is not constrained by imposing tendencies of moisture and temperature.

A number of recent studies have used the WTG and WPG approximations to study convection in cloud resolving models (CRMs). In idealized WTG numerical simulations, researchers studied how convection responds to localized changes in sea surface temper-

atures [SST, *Sobel and Bretherton*, 2000], surface fluxes and wind speed [*Raymond and Zeng*, 2005; *Sessions et al.*, 2010; *Anber et al.*, 2014], wind shear [*Anber et al.*, 2014], radiation [*Anber et al.*, 2015], and changes in atmospheric stability and moisture [*Raymond and Sessions*, 2007; *Sobel and Bellon*, 2009; *Sessions et al.*, 2015; *Daleu et al.*, 2015; *Raymond et al.*, 2015]. A recent study [*Wang et al.*, 2013] benchmarked how significantly the WTG and WPG approximations reproduced diagnostics in MJO convection of the Tropical Ocean Global Atmosphere Coupled Ocean Atmosphere Response Experiment (TOGA-COARE). So far, no study has compared observations and modeling results to determine if observed relationships between convective and environmental diagnostics are preserved in models; that is the goal of this paper.

We compare diagnostic relationships hypothesized to be relevant to tropical convection in observations and WTG simulations. We use observations from the Dynamics of the Madden-Julian Oscillation (DYNAMO) field campaign [*Johnson and Ciesielski*, 2013; *Ciesielski et al.*, 2014a, b; *Johnson et al.*, 2015] to force and verify WTG simulations. This work is similar to a previous study that implemented observations into WTG and WPG simulations [*Wang et al.*, 2013], but there are some significant differences. For example, not only do we perform WTG simulations with domain averages from DYNAMO North and south Sounding Arrays, we also force WTG simulations with individual DYNAMO station soundings in order to benchmark the WTG approximation in more localized conditions. Probably the most important contribution of this work is a comparison between observed and modeled diagnostic relationships relevant to tropical dynamics. Identifying these relationships in observations is important for better understanding convection it-

self; determining whether these relationships are preserved in WTG experiments helps to validate the WTG approximation as a useful tool for understanding tropical convection.

This paper is organized as follows. In Section 2, we describe the model, the WTG approximation, observations used in the study, and the methodology. In Section 3 we compare observed and modeled diagnostic time series and relationships. In section 4 we present our conclusions, and in the appendix we present the details of verifying the modeled time series.

2. Model, observations and methodology

In this section we introduce the cloud resolving model (CRM), the WTG approximation, observations, and the methodology used in this study. The version of the WTG approximation we use is called the spectral weak temperature gradient approximation [SWTG, *Herman and Raymond*, 2014], and is described in section 2.1.

2.1. Model and the weak temperature gradient (WTG) approximation

We use the CRM of *Herman and Raymond* [2014]. The model solves the fully compressible non-rotating momentum equations on a double periodic two or three dimensional domain. Prognostic equations govern specific moist entropy, the precipitation mixing ratio, and the total cloud water mixing ratio. The prognostic variable entropy is used because of improved conservation properties [*Raymond*, 2013] compared to the customary moist static energy. The dry (s_d), moist (s), and saturated (s^*) entropy are defined

approximately as:

$$s_d = c_p \ln\left(\frac{\theta}{\theta_R}\right), \tag{1}$$

$$s = c_p \ln\left(\frac{\theta_e}{\theta_R}\right), \tag{2}$$

$$s^* = c_p \ln\left(\frac{\theta_e^*}{\theta_R}\right). \tag{3}$$

Here, c_p is the specific heat of dry air at constant pressure, $\theta_R = 300$ K is a reference temperature, and θ, θ_e, and θ_e^* are the potential, equivalent potential, and saturated equivalent potential temperatures, respectively. The model uses simplified microphysics and radiation [*Raymond*, 2001], and boundary layer turbulence is parameterized by Monin-Obukhov similarity theory. Please refer to *Herman and Raymond* [2014] for a detailed description of the model.

The CRM represents a limited region of the tropical atmosphere, and interacts with a specified reference environment through the WTG approximation. The conventional WTG approximation is based on the ideas from observations [*Bretherton and Smolarkiewicz*, 1989], and scaling arguments [*Charney*, 1963; *Sobel and Bretherton*, 2000] that gravity waves quickly redistribute heating anomalies, and leave weak horizontal temperature gradients in the tropics. Parcels with redistributed heat lift adiabatically and cool, equilibrating the system. In a model with periodic boundary conditions, like the one we are using, potential temperature anomalies due to latent heat release and radiative cooling are trapped in the domain. In order to mimic the real world process, the model generates a vertical velocity, called the WTG vertical velocity:

$$w_{wtg}(z,t) = \frac{D_\theta(z,t)M(z)}{\tau}, \tag{4}$$

where $D_\theta(z,t)$–interpreted as the height a parcel needs to reach to remove a heating anomaly–is given by:

$$D_\theta(z,t) = \frac{\bar{\theta}(z,t) - \theta_{ref}(z,t)}{\frac{\partial \bar{\theta}(z,t)}{\partial z}}. \tag{5}$$

Here, $\bar{\theta}(z,t)$ is the domain averaged potential temperature, $\theta_{ref}(z,t)$ is the reference profile of potential temperature, τ is a relaxation timescale by which the model potential temperature is relaxed to the reference potential temperature, and $M(z) = \sin(\pi z/h)$ is a masking that modulates the enforcement of the WTG approximation to the region between the surface and the tropopause (h, assumed 15 km). The WTG velocity is interpolated from the boundary layer height (assumed 1 km) to zero at the surface. Also, the relaxation time scale, τ, can be interpreted as the time it takes gravity waves to travel the domain length and is taken to be 1 h in this study.

Recently, *Herman and Raymond* [2014] proposed a modification of this conventional WTG approximation which accounts for the fact that different heating profiles result in gravity waves of different speeds [*Bretherton and Smolarkiewicz*, 1989]. In contrast to the conventional WTG approximation–which assumes one phase speed for all wave numbers of buoyancy waves–the spectral WTG (SWTG) does a Fourier decomposition of the heating anomaly and assigns each wave number a corresponding phase speed:

$$c_j = N/m_j, \tag{6}$$

where N is the Brunt-Väisälä frequency, and m_j is the vertical wave number mode. In SWTG, the equivalent height, $D_\theta(z,t)$ can be written as:

$$D_\theta(z,t) = \sum_j \Theta_j(t) \sin(m_j z), \tag{7}$$

where

$$\Theta_j(t) = \frac{2}{h}\int_0^h D_\theta(z,t)\sin(m_j z)dz, \tag{8}$$

are the Fourier modes, and h is the tropopause height. The SWTG vertical velocity can then be written as:

$$w_{swtg}(z,t) = \sum_j \frac{\Theta_j(t)}{\tau_j}\sin(m_j z), \tag{9}$$

where

$$\tau_j = L/c_j = Lm_j/N = \pi Lj/hN, \tag{10}$$

is the relaxation time scale for each vertical wave number. In contrast to WTG where the user sets τ, the primary length scale L is the free parameter in SWTG, related to τ approximately by $L = \tau hN/\pi$. In this study, we will present SWTG simulations with $L =$ 171 km, which is roughly equivalent to $\tau = 1$ h in the conventional SWTG. Henceforth, we will refer to the SWTG as WTG for convenience.

WTG sources of entropy and mixing ratio due to enforcing WTG are given by:

$$S_{ent} = w_{wtg}\frac{\partial \bar{s}}{\partial z} + (\bar{s} - s_{ent})\frac{1}{\rho_0}\frac{\partial \rho_0 w_{wtg}}{\partial z}, \tag{11}$$

$$S_{r_t} = w_{wtg}\frac{\partial \bar{r}_t}{\partial z} + (\bar{r}_t - r_{t-ent})\frac{1}{\rho_0}\frac{\partial \rho_0 w_{wtg}}{\partial z}, \tag{12}$$

where ρ_0 is the domain average density, $\bar{s}$ and $\bar{r}_t$ are domain averaged moist entropy and total water vapor mixing ratio, and, depending on whether mass flux decreasess with height (mass export) or increases with height (mass import):

$$s_{ent}, r_{t-ent} = \begin{cases} \bar{s}, \bar{r}_t & \text{if } \frac{\partial \rho_0 w_{wtg}}{\partial z} < 0 \text{ (mass export)}, \\ s_{ref}, r_{t-ref} & \text{if } \frac{\partial \rho_0 w_{wtg}}{\partial z} > 0 \text{ (mass import)}, \end{cases} \tag{13}$$

where s_{ref} and r_{t-ref} are reference profiles of moist entropy and water vapor mixing ratio. The WTG sources are used in the moist entropy and total water vapor mixing ratio

equations to parameterize the effect of the environment on local modeled convection in the prognostic equations:

$$\frac{\partial \rho s}{\partial t} + \nabla \cdot (\rho \mathbf{v} s - K \nabla s) = \rho (S_{ss} + S_{sr} - S_{ent}), \tag{14}$$

$$\frac{\partial \rho r_t}{\partial t} + \nabla \cdot (\rho \mathbf{v} r_t - K \nabla r_t) = \rho (S_{rs} + S_{rp} - S_{r_t}), \tag{15}$$

where K is the eddy-mixing coefficient, $\mathbf{v}$ is the velocity vector, S_{ss} and S_{sr} are the source of moist entropy from surface fluxes and radiation respectively, S_{rs} is the total water vapor mixing ratio source due to surface fluxes, and S_{rp} is minus the conversion rate of cloud water to precipitation [details about these terms can be found in *Herman and Raymond*, 2014].

2.2. Observations and Diagnostic Variables

We use version 3a of the Colorado State University quality controlled observations from the DYNAMO field campaign [*Johnson and Ciesielski*, 2013; *Ciesielski et al.*, 2014a, b; *Johnson et al.*, 2015]. We also use high resolution radiosonde data from individual stations in the DYNAMO array [ARM AMF Radiosonde L3 Data for stations Male, Colombo, Gan, and Diego Garcia, and L3.1 for Research Vessels Revelle and Mirai; e.g. *Ciesielski et al.*, 2014a], positions of which are shown in figure 1. These observations are used for obtaining time dependent reference profiles of potential temperature, mixing ratio, and surface winds which are used to force the WTG simulations (see below).

The diagnostic variables we compare are precipitation rate, saturation fraction, instability index and gross moist stability (GMS). These diagnostics provide important information about the relationships between convection and the environment, and are significant in the context of the tropical atmosphere [*Bretherton et al.*, 2004; *Raymond et al.*, 2007;

Raymond and Sessions, 2007; *Gjorgjievska and Raymond*, 2014; *Sessions et al.*, 2015; *Raymond et al.*, 2015]. Precipitation rate is a direct measure of convective activity, while saturation fraction–defined as precipitable water divided by saturated precipitable water–diagnoses the moistening effects of convection, with larger values corresponding to moister air columns. The instability index diagnoses the stability of air in the column. It is defined as [e.g. *Raymond et al.*, 2011; *Sessions et al.*, 2015]:

$$II = s^*_{low} - s^*_{high}, \tag{16}$$

where s^*_{low}, and s^*_{high}, are the horizontally averaged saturated moist entropy integrated from 1-3 km, and 5-7 km, respectively. Smaller values of the instability index correspond to a more stable column of air.

Neelin and Held [1987] introduced the GMS as a variable that quantifies the relationship between convection and convective forcing in absence of the details of the nature of the relationship. GMS is defined as a ratio of export of a quantity conserved in moist processes, and import of a quantity that measures strength of convection [see *Raymond et al.*, 2009, for a comprehensive overview of GMS]. In this work we calculated GMS from observations, Γ_{obs}, analogous to *Sobel et al.* [2014], as the ratio of moist and dry entropy divergence:

$$\Gamma_{obs} = \frac{\left\langle \omega \frac{\partial s}{\partial p} + \mathbf{v} \cdot \nabla s \right\rangle}{\left\langle \omega \frac{\partial s_d}{\partial p} \right\rangle}, \tag{17}$$

where ω is the vertical velocity in pressure coordinates, and the brackets denote vertical pressure integral from surface to 100 hPa. Also, we neglect the horizontal part of dry entropy divergence as in *Inoue and Back* [2015a].

In calculating GMS from numerical output, the WTG velocity takes the place of large scale vertical motion, and the lateral import or export of moist entropy and total mixing

ratio is dependent on the layers where mass flux is positive or negative respectively. The model GMS is defined as:

$$\Gamma_{mod} = \frac{\langle S_{ent} \rangle}{\left\langle w_{wtg} \frac{\partial s_d}{\partial z} \right\rangle}, \tag{18}$$

where S_{ent} is the source of moist entropy due to the WTG approximation (equation 11), and the brackets denote mass weighted height integral from the surface to the tropopause (15 km, around 100 hPa).

2.3. Methodology

We study the relationships between the observed and modeled DYNAMO diagnostics using the following procedure:

1. We run the model in non-WTG mode, with interactive radiation, until it reaches a state of radiative-convective equilibrium (RCE, i.e convective forcing balances radiative cooling). For the RCE simulation, we use an SST of 302 K, which is the average SST in the DYNAMO intensive observation region (see below). We set the surface wind speed to 2 m s^{-1}, which is the average surface wind speed–here defined as the wind speed at the lowest level–during DYNAMO, and run the model on a 2D model domain 200 km long (1 km horizontal resolution) and 20 km high (250 m vertical resolution); the WTG simulations use the same model geometry as the RCE simulations. We obtain RCE potential temperature and total water mixing ratio profiles by averaging the last thirty days of a fifty day RCE simulation.

2. Observed potential temperature and mixing ratio anomalies, which represent changes in environmental conditions, are obtained by subtracting the time mean temperature and water vapor mixing ratio profile from the observational time series. We obtain anomalies for both DYNAMO array averaged profiles (North Sounding Array, NSA, and South

Sounding Array, SSA), and six individual sounding stations that compose NSA and SSA arrays (Male, Colombo, Gan, Diego Garcia, and Research Vessels Revelle and Mirai, see figure 1 for positions).

3. Finally, time dependent reference profiles for WTG simulations are obtained by adding the observed DYNAMO potential temperature and water vapor mixing ratio anomalies (interpolated on the model grid) to the RCE profiles of potential temperature and mixing ratio.

4. In addition to the WTG reference profiles, observed surface wind speed and SST variations are imposed in the WTG simulations. We do not consider the effects of shear and radiation in this study; we specify a non-interactive static cooling rate derived from the RCE simulation.

For the NSA and SSA sounding arrays, we imposed daily SST variations derived from ERA-I [*Dee et al.*, 2011] since we lacked complete and representative surface observations [*Wang et al.*, 2014]. Lacking SST observations for the single station simulations, we used an SST of 302 K (the average value from NSA and SSA derived from ERA-I). This treatment is justified since sensitivity studies (not shown) on NSA and SSA stations showed that removing or doubling SST variations did not have a significant impact on WTG results.

In addition to a qualitative comparison of observed and modeled diagnostic time series, we compare them quantitatively by computing statistical quantities such as correlation coefficients (with t-student tests for significance levels), mean, and standard deviation; these are presented in the appendix. Since GMS is a sensitive variable, especially in numerical simulations, the time series data is smoothed with a five day moving average before daily

averaging the time series; global characteristics of the diagnostics are preserved despite the loss in detail.

3. Results and discussion

In this section we first compare time series in observed and modeled DYNAMO diagnostics. The time series were smoothed with a five day moving average in order to focus on large time scales and processes that influence the development of convection in DYNAMO [*Sobel et al.*, 2014; *Inoue and Back*, 2015b]. Next, we compare observed and modeled diagnostic relationships and, where possible, compare them with past work. Here we do three sets of comparisons for each diagnostic relationship: observations with model, the NSA with the SSA, and arrays with the single stations. Details about time series for single station WTG simulations can be found in the appendix.

3.1. Diagnostic time series

Figure 2 shows the NSA and the SSA observed (black) and modeled (red) time series of precipitation rate (panels a–b), saturation fraction (panels c–d), instability index (panels e–f), and GMS (panels g–h), smoothed with a five day moving average. Despite the applied smoothing, trends in both observed and modeled time series are preserved. Also, after smoothing the GMS denominator and numerator, time periods where denominator is less than one fifth of the numerator have been removed, similar to *Sobel et al.* [2014], to avoid division by zero. For the reader's convenience, as rough guidelines, vertical dashed lines are aligned with precipitation maxima in the NSA, at days 25, 56, and 81.5. Despite the fact that precipitation maxima occur at different times for the NSA and the SSA, we use the NSA guidelines in the SSA plot for comparison.

3.1.1. Comparison of observations and simulations

Figure 2 shows three distinct precipitation intense events around 25, 56 and 81.5 days for the NSA, all of which are approximately captured by the model. Compared to the NSA, the SSA has less intense precipitation rates with maxima that lag the NSA maxima for the first two events. The precipitation rate increase prior to the NSA precipitation maxima is correlated with an increase in saturation fraction and a decrease in instability index, both in observations and simulations (though the relationship is not equally strong for every precipitation event, see e.g. first event in the SSA). The inverse holds for decrease of precipitation rate with time; after the precipitation maxima, saturation fraction decreases and instability index increases. This behavior is in agreement with a thermodynamic mechanism proposed in previous idealized WTG simulations and observations [*Raymond and Sessions*, 2007; *Gjorgjievska and Raymond*, 2014; *Sessions et al.*, 2015; *Raymond et al.*, 2011, 2014, 2015]. This mechanism posits that changes in the atmospheric stability (quantified here via the instability index) result in changes to the convective profile, which in turn adjusts the vertical advection and lateral entrainment of moisture (quantified by saturation fraction). A decrease in the instability index (i.e. a more stable environment) causes more bottom heavy mass flux profiles which entrain moister lower tropospheric air, and consequently increases the saturation fraction. An increased saturation fraction, in turn, results in higher precipitation rates, which has been confirmed in a number of studies [*Bretherton et al.*, 2004; *Raymond et al.*, 2007; *Masunaga*, 2012].

The saturation fraction and instability index peak and dip, respectively, in phase with peak precipitation rates, with significant differences in observed and modeled mean magnitudes. The discrepancy between modeled and observed saturation fraction and instability

index could arise in part because of model parameters (e.g. dimensionality, microphysics, etc.), and the RCE profiles used in the WTG reference profiles. The parameters used in the model [*Raymond and Zeng*, 2005] are, approximately, standard values found in the tropics, which might vary with geographic location. Alternatively, the model might be missing an essential mechanism for modeling DYNAMO convection. Here, we restrict our discussion to the possible influence of the model setup to explain the discrepancy between observed and modeled saturation fraction and instability index, while possible mechanism deficiencies are beyond the scope of this study.

The discrepancy between observed and modeled saturation fraction and instability index might arise because of the RCE profiles used in the WTG reference profiles–computed using ERA-I SST averaged over the NSA and the SSA domains. However, model parameters and dimensionality of the computation domain [*Wang and Sobel*, 2011] influence significant differences between the RCE and observed mean potential temperature and moisture. Figure 3 shows the difference between the observed (black) and modeled (RCE, red) mean potential temperature (panel a) and water vapor mixing ratio (panel b). The RCE profile is cooler and shows a slightly smaller lapse rate than observations which results in a smaller instability index compared to the observed mean profile. On the other hand, the RCE simulation is drier than the observed; the model, however, exhibits a higher saturation fraction because the more stable RCE environment more efficiently entrains environmental air [*Raymond and Sessions*, 2007; *Sessions et al.*, 2015]. Sensitivity studies (not shown) revealed that using RCE profiles of potential temperature and mixing ratio closer to the observed mean (e.g. using RCE profiles from SST of 304 K, shown with a red dashed line in figure 3), decreases the difference between observed and mod-

eled saturation fraction and instability index. However, the general results of this paper are not affected by this issue, and, for consistency, we choose to use the RCE profiles corresponding to the reanalysis SSTs.

Previous work [*Ciesielski et al.*, 2014b; *Sobel et al.*, 2014] has addressed the energy budget in DYNAMO, and proposed mechanisms that control the development of convection. In an analysis of the moist static energy budget, *Sobel et al.* [2014] concluded that the effects of radiation and surface fluxes exert the dominant control of convection during DYNAMO However, convection may evolve as a result of changes to the atmospheric stability, which may be a consequence of changes in radiation and surface fluxes, and–by modification of the convective profile–would influence the vertical and horizontal advection of moist static energy. Alternatively, *Inoue and Back* [2015a] examined TOGA COARE data and found that vertical and horizontal advection of moist static energy is important for the development and decay of convection, and that radiation and surface fluxes act to destabilize convection throughout convective events. The effects of horizontal and vertical transport of convection can be summarized by the gross moist stability (GMS), and we address them next.

3.1.2. Gross Moist Stability (GMS)

GMS summarizes the effects of large scale interactions on convection; understanding what controls GMS can lead to a better representation of convection in coarsely resolved models.

The observed GMS (figure 2g–h) increases from small and even slightly negative values during developing convection (periods of increasing precipitation rate, prior to precipitation maxima on days 25, 56 and 81.5), and it continues to increase for dissipating

convection (decreasing precipitation rate, after the precipitation maxima). The model GMS behaves similarly, but with a magnitude that is smaller than the observed at peak precipitation rates. Despite this difference in magnitude, the modeled GMS also shows an increase similar to the observed GMS, relative to the GMS values at peak precipitation rates; GMS increases throughout the life cycle of the convective event.

This GMS behavior has been addressed in a recent study. Based on TOGA-COARE data, *Inoue and Back* [2015a] developed a theory for convective development and decay relative to a characteristic GMS value:

$$\Gamma_C = \frac{\langle Q_R \rangle + \langle SF \rangle}{\langle \nabla \cdot (s_d \vec{v}) \rangle}, \tag{19}$$

where Q_R and SF are radiative and surface flux forcing, respectively, and $\nabla \cdot (s_d \vec{v})$ is the divergence of dry entropy. The authors show that convective development (precipitation increases with time) occurs for GMS values lower than Γ_C–which turns out to be approximately constant during TOGA COARE [*Inoue and Back*, 2015a]–while convective decay (precipitation decreases with time) happens for GMS values higher than Γ_C. This behavior can be seen for some of the convective events in figure 4a–b, which shows the GMS (from figure 2g–h, thick lines), and the characteristic GMS (Γ_C, thin lines) for the observations and the model; for comparison, the dashed vertical lines represent the NSA precipitation maxima. The model follows the theory and observations from *Inoue and Back* [2015a]; Γ_C remains fairly constant, and $\Gamma < \Gamma_C$ for developing modeled convection, and $\Gamma > \Gamma_C$ for decaying modeled convection. A particularly nice model example is seen on days 50–60. The observed Γ_C, on the other hand, deviates somewhat from the theory; at times the observed GMS is in phase with Γ_C, while at times it shows behavior opposite

to that of *Inoue and Back* [2015a]. This discrepancy might be influenced by noise in the observational data, analysis of which is beyond the scope of this study.

In addition to the usefulness of the characteristic GMS time series in studying the dynamics of convection, calculating a characteristic value for a particular data set can also be useful. *Inoue and Back* [2015a] list several different methods for calculating the characteristic GMS found in the literature; here we redefine them in terms of moist entropy instead of moist static energy. According to *Inoue and Back* [2015a], the characteristic GMS can be calculated as:

1. GMS at maximum anomalous precipitation:

$$\Gamma'_{max} \equiv \Gamma|_{P_{max}}, \tag{20}$$

2. GMS computed from a scatter plot of anomalous $\nabla \cdot \langle s\mathbf{v} \rangle$ versus $\nabla \cdot \langle s_d\mathbf{v} \rangle$:

$$\tilde{\Gamma'} \equiv \frac{\overline{< \nabla \cdot (s\mathbf{v}) >' \cdot < \nabla \cdot (s_d\mathbf{v}) >'}}{\overline{(< \nabla \cdot (s_d\mathbf{v}) >')^2}}, \tag{21}$$

3. GMS computed from a scatter plot of non-anomalous $\nabla \cdot \langle s\mathbf{v} \rangle$ versus $\nabla \cdot \langle s_d\mathbf{v} \rangle$:

$$\tilde{\Gamma} \equiv \frac{\overline{< \nabla \cdot (s\mathbf{v}) > \cdot < \nabla \cdot (s_d\mathbf{v}) >}}{\overline{(< \nabla \cdot (s_d\mathbf{v}) >)^2}}, \tag{22}$$

4. and, GMS in a quasi-steady state:

$$\Gamma_0 \equiv \frac{\overline{< \nabla \cdot (s\mathbf{v}) >}}{\overline{< \nabla \cdot (s_d\mathbf{v}) >}}. \tag{23}$$

In this paper, we calculate the characteristic GMS, Γ_C, using each of these methods for both the NSA and the SSA in modeled and observed data. These results are shown in Table 1. Both the NSA and the SSA have characteristic GMS values close to 0.4, across all of the definitions. The modeled values, on the other hand, show more variability across the four definitions, and range from 0.1 to 0.2, with the SSA leaning toward higher values. We

address the non-trivial difference between the observed and modeled characteristic GMS below, and in section 3.2.

The difference between the observed and modeled characteristic values can be analyzed by decomposing the GMS into contributions from vertical, Γ_V, and horizontal, Γ_H, motions. To accommodate the coordinate systems of the observational and model data set, we have:

$$\Gamma_{obs-V} = \frac{\langle \omega \frac{\partial s}{\partial p} \rangle}{\left\langle \omega \frac{\partial s_d}{\partial p} \right\rangle}, \tag{24}$$

$$\Gamma_{obs-H} = \frac{\langle \mathbf{v} \cdot \nabla s \rangle}{\left\langle \omega \frac{\partial s_d}{\partial p} \right\rangle}, \tag{25}$$

for the observations, and:

$$\Gamma_{mod-V} = \frac{\langle w_{wtg} \frac{\partial \bar{s}}{\partial z} \rangle}{\langle w_{wtg} \frac{\partial s_d}{\partial z} \rangle}, \tag{26}$$

$$\Gamma_{mod-H} = \frac{\langle (\bar{s} - s_{ent}) \frac{1}{\rho_0} \frac{\partial \rho_0 w_{wtg}}{\partial z} \rangle}{\langle w_{wtg} \frac{\partial s_d}{\partial z} \rangle}, \tag{27}$$

for the model (see term definitions in sections 2.1 and 2.2). Figure 4 (panels c–f) show the horizontal and vertical components of the GMS numerator; they differ in magnitude, both for the observations and the model. The NSA horizontal transport of moist entropy (panel c) is about an order of magnitude smaller than the vertical transport (panel e) during intense precipitation periods; the difference is smaller for the SSA (panels d and f). This indicates the importance of the vertical transport in the development of convection in DYNAMO, and it is in agreement with *Inoue and Back* [2015a]. The source of the difference in the observed and the modeled GMS magnitudes seen in figure 4a,b can be seen in figure 4e,f; the model consistently underestimates the vertical transport of moist entropy compared to observed values.

The observed and modeled GMS denominator (figure 4g,h) are in excellent agreement for the NSA, while it is generally slightly underestimated for the SSA. The success of the model in reproducing the denominator–the divergence of the dry entropy, $w_{wtg}\partial s_d/\partial z$–is directly related to enforcement of the WTG approximation. In the WTG approximation the vertical gradient of the dry entropy, $\partial s_d/\partial z$, is constrained explicitly by the relaxation of the temperature to the reference environment. The WTG vertical velocity, w_{wtg}, on the other hand, is not explicitly constrained and is calculated according to equation 4 or 9. Since the model captures the trends in the observed denominator, this indicates that the WTG approximation is adequately capturing the variations in the large scale vertical velocity. On the other hand, the weaker denominator for the SSA indicates that the modeled SSA vertical advection is too weak, and could possibly be adjusted by fitting the time scale τ or length scale L. The difference between the NSA and the SSA WTG simulations might indicate differing dynamics in the two regions during DYNAMO, and may provide clues as to which are well represented by WTG.

3.1.3. Possible sources of stability changes.

So far our results suggest, in conjunction with previous work [*Raymond and Sessions*, 2007; *Sessions et al.*, 2015; *Raymond et al.*, 2015], that increased atmospheric stability (quantified by lower instability index) increases the moisture content (quantified by higher saturation fraction), and consequently increases the precipitation rate. Since the WTG simulations are forced by atmospheric stability changes–changes in the reference potential temperature profiles–the question of the sources of those changes arises.

In a recent paper, *Raymond et al.* [2015] develop a hypothesis relating the interplay of dynamics and thermodynamics in tropical convection. Given an evolution of the poten-

tial vorticity field with necessary boundary conditions and a balance condition–nonlinear balance, in case of the tropics– one could deduce the evolution of atmospheric stability, via changes to the virtual temperature [which are closely related to changes in potential temperature, e.g., see *Raymond et al.*, 2014]. We do not know if this type of balanced dynamics is at work in the DYNAMO MJO, and although this data deserves a full analysis in this context, we present preliminary results which relate some of the diagnostics used from *Raymond et al.* [2015] to the dynamics in the DYNAMO MJO. Specificaly, we explore the possibility that there is a relationship between the vorticity and divergence in this case, as hypothesized for tropical convection [*Raymond et al.*, 2015].

Figure 5 shows budget derived [*Johnson and Ciesielski*, 2013; *Ciesielski et al.*, 2014a, b; *Johnson et al.*, 2015] time series of divergence and vorticity–smoothed with a five day moving average–for the NSA and the SSA. Here, we focus only on observations since the idealized setup of WTG simulations does not capture large scale vorticity and divergence. The variables were averaged vertically in layers–0-15 km, 0-3 km, 3-8 km, and 8-15 km–in order to analyze the vertical structure of vorticity and divergence, and to speculate on possible correlation with stability changes. Despite the fact that the tropospheric vertical average from 0 to 15 km (black solid line) shows no features which might correlate with stability changes, significant patterns emerge when we divide the troposphere into layers.

Both for the NSA and the SSA divergence (figure 5, panels a–b) shows strong positive values in the upper levels (8-15 km), signifying mass export, while weaker negative values of divergence occur at mid (3-8 km) and low (0-3 km) levels simultaneously, signifying mass import. Compared to the vorticity (panels c-d) the divergence is much stronger,

especially in the upper levels. Despite the fact that the divergence is much stronger than vorticity, divergence patterns show uniformity across the different convective events.

The vorticity, on the other hand, distinguishes differing dynamics between the first, second, and third convective events both in the NSA and the SSA. In the NSA, the first event (days 15–35), shows little vortical activity during the peak precipitation rate period from days 25–30. Vorticity shows patterns, however weak, during the developing (days 15–25) and decaying (days 30 -35) phases of the first convective event. The vertical structure shows a dipole (negative vorticity at low levels, positive vorticity aloft) in the developing and the decaying phase; the weakness of the vorticity makes it hard to distinguish the vorticity significantly different than zero, so we cannot speculate on the dynamics of these vorticity features. For the second NSA event (days 50–60) the low and mid level vorticity show a prominent peak around the precipitation rate maximum, which could be associated with the atmospheric stability changes and convective development during that period. The second vorticity anomaly might be associated with a passing cyclone visible in infrared satellite imagery (not shown). The third precipitation event shows persistent surface vorticity with a developing mid level vortex which peaks around the precipitation maximum.

The SSA shows similar conditions with some major differences; apart from the fact that the SSA is on the southern hemisphere so that the vorticity bears, in general, the opposite sign compared to the NSA. The first precipitation event is accompanied by a persistent vorticity dipole from days 10–40. The constancy of this vorticity dipole might be associated with the moderate persistent precipitation rates from days 10-30, while the development of the mid level vorticity around day 33 might be associated with decay of

the convection. The second SSA precipitation event is associated with strong vorticity in low and mid levels, similar to the NSA. Lastly, the third precipitation event shows similar conditions as the NSA, with vorticity bearing the opposite sign.

In conclusion, balanced vorticity dynamics might be associated with atmospheric stability changes, because of distinct patterns observed in the DYNAMO arrays. However, further work is necessary to confirm this hypothesis.

3.1.4. Individual stations in the DYNAMO array and WTG verification.

To obtain time series and verify the performance of the WTG approximation in simulating the convection during DYNAMO, we compared observed and modeled daily averaged time series of precipitation rate, saturation fraction, and instability index for WTG applied to individual stations in DYNAMO. It is useful to compare these with the results from the NSA and the SSA so that we have a measure for how well WTG performs using observations over different spatial scales. This result might help interpret WTG results from data taken from isolated soundings from field campaigns that do not have an ordered configuration of arrays like DYNAMO or TOGA COARE. A detailed account of the verification of WTG simulations on both station arrays (the NSA and the SSA), and individual stations, can be found in the Appendix.

In general, our comparisons of modeled and observed convective diagnostics for both regional arrays and single stations show that the WTG approximation qualitatively and quantitatively does a good job in reproducing the observed diagnostics with at least some of the differences accountable to the model parameters (e.g. microphysics and RCE profiles used in WTG reference profiles as explained above). There are some differences, however, that are not easily attributable to model parameters, which suggests that other

mechanisms which do not act through the thermodynamic environment are also important for modulating tropical convection. Although understanding what these are is important for improving convective parameterizations, a systematic analysis is beyond the scope of this study.

3.2. Diagnostic relationships

In this section we consider diagnostic relationships between precipitation rate, saturation fraction, instability index, and GMS. The relationship between these diagnostics has been studied in satellite observations as well as in models in past work. For example, *Bretherton et al.* [2004], and *Raymond et al.* [2007] have proposed a strong relationship between precipitation rate and saturation fraction. Also, numerical studies by *Raymond and Sessions* [2007], *Sessions et al.* [2015], and *Raymond et al.* [2015] showed a strong dependence of the saturation fraction on the stability of the column air. We compare diagnostic relationships derived from observations and WTG simulations to see how significant the relationships are in observed data, and test if the WTG approximation preserves the diagnostic relationships. We do so for the NSA, the SSA, and all the results from the single station simulations.

Figure 6 shows observed (blue and black) and modeled (red) relationships between precipitation rate and saturation fraction (panels a–c), precipitation rate and instability index (panels d–f), and saturation fraction and instability index (panels g–i), for the NSA (panels a, d, and g), the SSA (panels b, e, and h), and the single station simulations (panels c, f, and i). We divided the observed data into two regimes because of distinctive behavior in observed relationships; events with precipitation rates lower than P_B, and saturation fraction less than S_B (gray shaded area in panels a–c) are colored blue, while

the remaining data is colored black. We choose $P_B = 5$ mm day^{-1}, and $S_B = 0.73$ somewhat arbitrarily, but our choice does not qualitatively affect our results. We explain the reasons for this separation in detail below.

For qualitative comparison with previous research, we overlay the precipitation rate–saturation fraction functional relationships (figure 6a–c) from *Bretherton et al.* [2004, dashed blue]:

$$P(S) = \exp[b(S - S_D)], \tag{28}$$

where S is saturation fraction, and the numbers $b = 15.6$, and $S_D = 0.603$, are fitting parameters, and from *Raymond et al.* [2007, solid blue];

$$P(S) = R_{RCE} * \frac{S_C - S_{RCE}}{S_C - S}, \tag{29}$$

where the number $S_C = 0.87$ is a fitting parameter, and $R_{RCE} = 4$ mm day^{-1} and $S_{RCE} = 0.81$ are steady state precipitation rate and saturation fraction for an RCE simulation. For the saturation fraction–instability index relationship (figure 6g–i) we overlay [*Raymond et al.*, 2015, solid blue]:

$$S(II) = c * II + d, \tag{30}$$

where II is the instability index, and $c = -0.00433$, and $d = 0.897$ are fitting parameters. For quantitative comparison with previous work, we perform exponential and linear fits for the precipitation rate–saturation fraction and saturation fraction–instability index relationships, respectively, for the observations (dashed black curves) and model (dashed red curves). Table 2 lists the fit parameters with 95% confidence intervals, together with fit parameters for relationships from previous work for comparison.

Precipitation rate–saturation fraction relationship. The precipitation rate (figure 6a–c) increases with saturation fraction for both the average arrays and for all the single station simulations. The observed NSA and SSA precipitation rate–saturation fraction scatters follow both the fit line (black dashed line) and the satellite observational fit from *Bretherton et al.* [2005, equation 28, blue dashed line], while the model scatter–and its exponential fit (red dashed line)– is closer to the *Raymond et al.* [2007, equation 29] power law relationship; qualitatively it seems that the modeled relationship might follow an exponential form. Quantitative conclusions on whether this relationship follows exponential or power law forms is beyond the scope of this study; the number of DYNAMO observations might be to small to make a statistically significant conclusion. Furthermore, the SSA relationship for both model and observations seem to follow the NSA relationships but do not extend to higher precipitation rates. Indeed, fit parameters for the precipitation rate–saturation fraction relationship (table 2) are similar for the NSA and the SSA, within variability, for both the observations and the model. In contrast to the NSA and the SSA, the single station observations and simulations show more scatter. One possible reason for less scatter in the NSA and SSA relationships might be the smoothing effect of the objective analysis used to interpolate data sets [*Johnson and Ciesielski*, 2013; *Ciesielski et al.*, 2014a] before they were averaged. Despite the scatter, however, the single station precipitation rate is a strong function of saturation fraction, similar to the NSA and the SSA, for both the observations and the model (table 2, and figure 6a–c). This is the most important point of this result.

Both the model and observed data seem to have better fits to the exponential forms [equation 28 *Bretherton et al.*, 2005] than to the inverse relation with with the saturation

deficit [equation *Raymond et al.*, 2007]. We note that the *Raymond et al.* [2007] relation was obtained from idealized steady state WTG simulations; deviations from this may arise as a result of transient dynamics. Furthermore, the NSA and the SSA observations are averaged over a larger area, similar to satellite measurements. Other studies with satellite data [*Masunaga*, 2012] have shown that the precipitation rate–saturation fraction relationship is time dependent, and that it changes for different orders of convective organization.

Precipitation rate–instability index relationship. The precipitation rate increases with decreasing instability index (figure 6d–f) for the NSA, the SSA, and all the single stations. The NSA shows this prominently for both the observations and the model. However, the NSA also exhibits events with low precipitation rate for low instability index, which the model does not capture. These outliers fall into the region of precipitation rates lower than 5 mm day^{-1} and saturation fractions lower than 0.73 (gray shaded region in figure 6a–c). This behavior suggests that the WTG approximation does not capture a mechanism which inhibits precipitation events for increased stability (i.e. decreased instability index) of the outliers. We find similar behavior in the SSA though the relationship in the SSA is much less obvious. Compared to the NSA and the SSA, the single station simulations also show more variance in atmospheric stability for low rain rates. Nevertheless, they still show a general increase in precipitation for more stable environments, consistent with the balanced dynamics hypothesis of *Raymond et al.* [2015].

As discussed in section 3.1.3, the balanced dynamics hypothesis explains how precipitation rate increases for lower instability index. A more stable atmosphere (quantified by a lower instability index) produces more bottom heavy mass flux profiles which entrain

more moist air from the low levels [*Raymond and Sessions*, 2007; *Raymond et al.*, 2011; *Gjorgjievska and Raymond*, 2014; *Raymond et al.*, 2014; *Sessions et al.*, 2015; *Raymond et al.*, 2015]. This increases the saturation fraction, and consequently the precipitation rate (figure 6a–c). Data for low precipitation rates and low saturation fractions do not seem to follow this general trend (blue dots, figure 6d–f), perhaps because of dry air intrusion that suppresses saturation fraction and therefore precipitation rates in more stable environments (this, however, has not been tested).

Saturation fraction–instability index relationship. The saturation fraction, in general, increases with lower instability index (figure 6g) in the NSA, both for the model and the observations. The outliers from the observed precipitation rate–instability index relationship were excluded before fitting a linear relationship on the data (table 2) for comparison with the modeled relationship. The WTG approximation captures the observed strong dependence of saturation fraction on instability index, for high saturation fraction events. For comparison, we overlaid the relationship from *Raymond et al.* [2015, solid blue], so far the only such relationship in the literature, which was derived for tropical cyclogenesis data for regions between 10 and 25 degrees in the Pacific and North Atlantic (THORPEX Pacific Asian Regional Campaign, T-PARC, Tropical Cyclone Structure-08, TCS-08, and the Pre-Depression Investigation of Cloud-Systems in the Tropics, PREDICT), there is no a priori reason for it to hold at the equator, or to hold for the DYNAMO convection which might differ in controlling mechanisms. However, this comparison shows that the saturation fraction–instability index relationship derived from DYNAMO data is a more sensitive function of the instability index than the cyclogenesis results from T-PARC, TCS-08 and PREDICT. It would be interesting to de-

termine if this was a consequence of latitude or different dynamics related to cyclogenesis compared to the MJO.

The SSA observations (figure 6h) differ from the NSA observations. There is more scatter in the SSA, and the outliers with precipitation rates lower than P_B and saturation fractions lower than S_B, do not separate neatly; there are precipitation events greater than P_B for saturation fractions lower than S_B. This scatter produces a more uncertain slope for the SSA observational fit (table 2, coefficient c for the SSA). The model fit, on the other hand, shows behavior similar to the NSA fit, with a slightly lower slope. The differences between the NSA and the SSA in all of the relationships so far, suggest a distinct feature; the WTG approximation seems to model the NSA region better than the SSA. The NSA experiences in stronger precipitation rates which the WTG approximation captures, which might indicate that the WTG approximation works better in organized convection if we take the intensity of precipitation to be a measure of convective organization.

As expected, the single station observations (figure 6i) show more scatter than the NSA and the SSA. Here, similar to the SSA, the outliers with precipitation rates lower than P_B and saturation fractions lower than S_B, exist for a wide range of the instability index. The scatter affects the linear fit for the observations in a similar manner as in the SSA; the correlation is weaker, and the slope is even lower than in the SSA. The scatter in the single station simulations might also reflect differences in local conditions for the individual stations.

Gross moist stability relationships. Given the existence of a characteristic GMS value related to peak precipitation rates [*Inoue and Back*, 2015a], we consider the relationship between the GMS and the precipitation rate, the saturation fraction, and the

instability index. This can give us clues as to how the GMS is related to the convective development and decay in DYNAMO.

Figure 7 shows precipitation rate–GMS (panels a–b), saturation fraction–GMS (panels c–d), and instability index–GMS (panels e–f) relationships, for the NSA (panels a, c, and e), and the SSA (panels b, d, and f). We did not calculate the single station GMS relationships because it is impossible to calculate divergences for single point soundings. The scatter plot of precipitation rate and GMS shows the non-negative characteristic GMS value–here defined as the value of GMS at maximum precipitation rate–in observations and simulations, both in the NSA, and the SSA. We calculate the characteristic value as the average GMS for precipitation rates greater than 10 mm/day, and mark it in the figure as a vertical dashed line (black for observations, red for model). This derived characteristic GMS value is also shown on remaining scatter plots in figure 7 for comparison, for the NSA and the SSA, respectively. For comparison with figure 6, events with precipitation rates less than P_B, and saturation fractions less than S_B, are shown in blue.

Although the precipitation–GMS relationship (panels a–b) is similar for the observations and the model; the characteristic GMS is different (0.41 for the observations, and 0.1-0.2 for the model). One possibility for this discrepancy is a consequence of the difference between the observed and the modeled (RCE) mean potential temperature and mixing ratio used in the WTG simulations. However, preliminary sensitivity tests (not shown) reveal that using RCE profiles closer to the observed mean profiles do not significantly affect the modeled characteristic GMS. An alternative reason for the discrepancy might be a result of either the surface fluxes or the radiation, according to one definition of the characteristic GMS (equation 19). Sensitivity simulations (not shown) indicate that

radiation effects–adjusted by changing the strength of the imposed RCE radiative cooling profile–does not affect the value of the characteristic GMS; the divergence of dry entropy adjusts to preserve the characteristic GMS value of 0.1-0.2. Given that neither the reference thermodynamic environment or radiation seem to affect the characteristic value of the GMS, it would be interesting to further investigate what sets this characteristic value.

The saturation fraction–GMS (figure 7c–d) and instability index–GMS (figure 7e–f) relationships show behavior similar to the precipitation rate–GMS relationship. The peak saturation fraction and smallest instability index are aligned with the characteristic GMS value from peak precipitation rates (figure 7a–b) both for the observations and the model, though the result is much stronger in the modeled convection. The instability index–GMS relationship (figure 7e–f) is somewhat obscured by low precipitation rate and low saturation fraction events (shaded blue).

In conclusion, the characteristic GMS permeates the dynamics of convective development in the DYNAMO field campaign. We consider the instability index to be the independent variable in the WTG simulations: it is determined by the reference potential temperature profile, which in turn sets the convective profile which modulates the lateral import/export of moisture and moist entropy, thus controlling the saturation fraction, the GMS, and the precipitation rate. There is a strong relationship between the characteristic GMS and instability index, though further work is necessary to explain the link between the two.

4. Conclusions

In order to better understand how local convection interacts with large scale conditions, we compared diagnostic relationships in observations and weak temperature gra-

dient (WTG) simulations of Dynamics of the Madden-Julian Oscillation (DYNAMO) convection. First, we imposed observed variations of thermodynamic variables–potential temperature, water vapor mixing ratio, wind speed, and sea surface temperatures (SST)– in WTG simulations of the north sounding array (NSA), the south sounding array (SSA), and six individual stations from the DYNAMO campaign. By comparing precipitation rate, saturation fraction (which quantifies moisture content) and instability index (which quantifies atmospheric stability), we found that the model reproduces the observations reasonably well, both quantitatively and qualitatively, with some systematic differences. These differences are possibly attributable either to model parameters used to construct the WTG simulations, or to dynamics that are not captured in the WTG approximation.

Second, we compared diagnostic relationships between the precipitation rate, the saturation fraction, the instability index, and the gross moist stability (GMS, which quantifies the interaction between local convection and large scale conditions), in observations and simulations. We found that:

1. The observed precipitation rate-saturation fraction relationship agrees with previous work [*Bretherton et al.*, 2004; *Raymond et al.*, 2004]: precipitation rate is a strong function of saturation fraction. The model shows similar behavior.

2. The observed and the modeled precipitation rate–instability index relationship agree, and suggest that the precipitation rate is a sensitive function of atmospheric stability; a more stable environment (quantified by low instability index) precipitates more efficiently. Outliers to this relationship suggest that the WTG approximation does not capture dynamics which suppress precipitation in more stable environments which otherwise support strong precipitation. Alternatively, the relationship between precipitation rate and atmo-

spheric stability occurs in more organized convection where the WTG approximation seems to perform well.

3. The observed and the modeled saturation fraction–instability index relationships also agree; though, more so for the NSA than the SSA and the individual stations in DYNAMO, which suggests different dynamics or perhaps different degrees of organization in the NSA compared to the SSA.

4. The relationships between the GMS and the precipitation rate, the saturation fraction, and the instability index, show that the characteristic GMS value [*Inoue and Back*, 2015a] differs between the observations (0.41) and the model (0.1-0.2). However, the characteristic GMS value is ubiquitous to all of the diagnostics; maximum precipitation rates, saturation fractions, and minimum instability index values all occur at the characteristic GMS, both for the observations and the model.

Despite the differences in magnitudes, the modeled gross moist stability (GMS) captures the general characteristics of the observed GMS; in both the observations and simulations, the GMS goes from small and/or negative values in the developing stages of the convection, to larger positive values in the decaying phases of the strong convective events. In agreement with the theory of *Inoue and Back* [2015a], GMS smaller than the characteristic occurs during developing convection, GMS larger than the characteristic indicates decaying convection (at least in strong MJO events).

Combining the theory of *Inoue and Back* [2015a], and the effects of atmospheric stability on atmospheric moisture content and precipitation rates–described in section 3, and in *Raymond and Sessions* [2007], *Sessions et al.* [2015], and *Raymond et al.* [2015]–gives

us a possible picture of how local convection interacts with large scale changes in the DYNAMO campaign:

1. The stability of the environmental air sets the type of the convection, via the vertical structure of the mass flux profile; a more stable environment (quantified by lower instability index) produces more bottom heavy mass flux profiles [*Raymond and Sessions*, 2007; *Raymond et al.*, 2011, 2014; *Gjorgjievska and Raymond*, 2014; *Sessions et al.*, 2015; *Raymond et al.*, 2015].

2. The mass flux profile then sets the amount of moisture available for precipitation; a more bottom heavy mass flux profile vertically advects moister lower-tropospheric air while also importing more moist lower tropospheric air via mass convergence at low levels [*Raymond and Sessions*, 2007].

3. Finally, the amount of moisture (quantified by saturation fraction) sets the precipitation rate since precipitation rate is a sensitive function of saturation fraction [*Bretherton et al.*, 2004; *Raymond et al.*, 2004].

This dynamical relationship has been demonstrated in observations of tropical cyclogenesis [*Gjorgjievska and Raymond*, 2014], but also seems to hold for the data presented here. This suggests, at least in strong (presumably more organized) convection, balanced dynamics also plays a role in the DYNAMO convection. A loose end in this study is the initial source of stability changes which eventually results in stronger precipitation rates. *Raymond et al.* [2015] indicates a potential vorticity anomaly is responsible for inducing the stability changes–further work, however, is necessary to study this possibility.

Appendix A: Verification of Weak Temperature Gradient Simulations

We verify the WTG simulations using reference profiles from individual stations, in addition to reference profiles derived from array averages (as a reminder, we use the spectral WTG approximation in these simulations). The combination of high resolution radiosonde data and large scale satellite derived precipitation rate, necessary for validating the WTG approximation on single stations, was not available until the DYNAMO campaign. Verifying the WTG approximation with precipitation gauge data is hindered by coarseness of precipitation gauge coverage. That is why we use Tropical Rainfall Measurement Mission (TRMM) data in tandem with DYNAMO sounding measurements for verifying both the sounding array, and the single station simulations. The single station verification sets precedent for future studies for using the WTG simulations in cases where large arrays are not present, and only individual station soundings are available.

Figures 8, 9, and 10 show daily averaged observed and modeled precipitation rate, saturation fraction, and instability index, respectively, for NSA and SSA (panels a–b), and individual stations (panels c–h). Correlation coefficients for each observation–model pair are also given. Table 1 lists the mean and standard deviation for all observed and modeled diagnostics with corresponding lag 0 correlation coefficients. Figure 8 also shows, in the panel titles, the mean imposed wind speed with respective standard deviations, for comparison.

The NSA and the SSA precipitation rate (figure 8a–b), saturation fraction (figure 9a–b), and instability index (figure 10a–b) are well reproduced, with SSA precipitation rate and saturation fraction having a weaker correlation with observations (table 3). Modeled diagnostics for Male, Colombo, Gan, and Diego Garcia (figures 8, 9, and 10, panels c, d, e,

and g) have a stronger correlation with observations than those for R/V Revelle and Mirai (figures 8, 9, and 10, panels f and h; table 3). Looking at differences between observed and modeled diagnostics, the model sometimes underestimates stronger precipitation rates for Gan and Diego Garcia (figures 8, 9, and 10, panels e and g), which suggests that the WTG relaxation length scale (L) might depend on geographical location. The modeled precipitation rate at Male (figure 8c) is stronger than the observed, and R/V Revelle and Mirai precipitation rates (figure 8f,h) between the observations and the model are poorly correlated, possibly because the model imposed winds, which are derived from observations, are stronger than those at the other stations; surface fluxes might be overwhelming or amplifying WTG effects. Modeled saturation fraction and instability index are consistently larger and smaller, respectively, than observed; section 3.1.1 lists possible reasons for this discrepancy.

The poor correlation between observed and modeled diagnostics for stations R/V Revelle and Mirai (figures 8, 9, and 10) might come from processes that cannot be captured by the WTG modeling paradigm. Qualitatively and quantitatively, the Mirai modeled precipitation rate (figures 8h) follows observations well, except for a dry spell from day 15 to day 25. A possible reason for the model missing the dry spell might be because the model did not capture a process that lead to a non-precipitating state from days 15 to 25. Modeled deep convective inhibition (DCIN, not shown)–defined as the average moist entropy from 0 to 1.75 km subtracted from the average saturated moist entropy from 1.75 to 2 km– had low values while the observed DCIN was substantial, which supports the hypothesis that the model did not capture the process leading to a dry state. R/V Revelle (figures 8f) exhibits a similar behavior: after the first couple of days the model misses

the dry spell, and goes into a state that does not resemble the observed. Further study is necessary to confirm the source of this behavior; these outliers, however, do not affect the conclusions of this paper.

Acknowledgments. We thank Richard Johnson and Paul Ciesielski for the DYNAMO sounding and array data. We thank David Raymond, Michael Herman, Patrick Haertel, and Larissa Back for fruitful discussions. We would like to acknowledge high-performance computing support from Yellowstone (ark:/85065/d7wd3xhc) provided by NCAR's Computational and Information Systems Laboratory, sponsored by the National Science Foundation. The model data used in this study can be obtained by contacting the corresponding author (ssentic@nmt.edu). This work was supported by U. S. National Science Foundation Grants ATM-0352639, ATM-1021049, AGS-1056254, and AGS-1342001.

References

References

Anber, U., S. Wang, and A. Sobel (2014), Response of atmospheric convection to vertical wind shear: Cloud-system-resolving simulations with parameterized large-scale circulation. part i: Specified radiative cooling, *J. Atmos. Sci.*, *71*, 2976–2993, doi: 10.1175/JAS-D-13-0320.1.

Anber, U., S. Wang, and A. Sobel (2015), Effect of surface fluxes versus radiative cooling on tropical deep convection, *J. Atmos. Sci.*, submitted.

Back, L. E., and C. S. Bretherton (2006), Geographic variability in the export of moist static energy and vertical motion profiles in the tropical pacific, *Geophys. Res. Lett.*,

827 *33*, L17810, doi:10.1029/2006GL026672.

828 Benedict, J. J., E. D. Maloney, A. H. Sobel, and D. M. W. Frierson (2014), Gross
829 moist stability and MJO simulation skill in three full-physics GCMs, *Journal of the*
830 *Atmospheric Sciences*, *71*(9), 3327–3349, doi:10.1175/Jas-D-13-0240.1.

831 Bretherton, C. S., and P. K. Smolarkiewicz (1989), Gravity waves, compensating sub-
832 sidence and detrainment around cumulus clouds, *J. Atmos. Sci.*, *46*, 740–759.

833 Bretherton, C. S., T. Uttal, C. W. Fairall, S. E. Yuter, R. A. Weller, D. Baumgardner,
834 K. Comstock, R. Wood, and G. B. Raga (2004), The EPIC 2001 stratocumulus study,
835 *Bull. Am. Meteor. Soc.*, *85*, 967–977.

836 Bretherton, C. S., P. N. Blossey, and M. Khairoutdivnov (2005), An energy-balance
837 analysis of deep convective self-aggregation above uniform sst, *J. Atmos. Sci.*, *62*,
838 4273–4292.

839 Charney, J. G. (1963), A note on large-scale motions in the tropics,
840 *Journal of the Atmospheric Sciences*, *20*(6), 607–609, doi:10.1175/1520-
841 0469(1963)020<0607:ANOLSM>2.0.CO;2.

842 Ciesielski, P. E., H. Yu, R. H. Johnson, K. Yoneyama, M. Katsumata, C. N.
843 Long, J. Wang, S. M. Loehrer, K. Young, S. F. Williams, W. Brown, J. Braun,
844 and T. Van Hove (2014a), Quality-controlled upper-air sounding dataset for DY-
845 NAMO/CINDY/AMIE: Development and corrections, *Journal of Atmospheric and*
846 *Oceanic Technology*, *31*(4), 741–764, doi:10.1175/jtech-d-13-00165.1.

847 Ciesielski, P. E., R. H. Johnson, K. Yoneyama, and R. K. Taft (2014b), Mitigation
848 of Sri Lanka island effects in Colombo sounding data and its impact on DYNAMO
849 analyses, *Journal of the Meteorological Society of Japan. Ser. II*, *92*(4), 385–405,

doi:10.2151/jmsj.2014-407.

Daleu, C. L., S. J. Woolnough, R. S. Plant, D. J. Raymond, S. L. Sessions, A. H. Sobel, G. Bellon, S. Wang, A. Cheng, M. J. Herman, P. Peyrille, P. Siebesma, and D. Kim (2015), Intercomparison of methods of coupling between convection and large-scale circulation, *J. Geophy. Res.*, in preparation.

Dee, D. P., S. M. Uppala, A. J. Simmons, P. Berrisford, P. Poli, S. Kobayashi, U. Andrae, M. A. Balmaseda, G. Balsamo, P. Bauer, P. Bechtold, A. C. M. Beljaars, L. van de Berg, J. Bidlot, N. Bormann, C. Delsol, R. Dragani, M. Fuentes, A. J. Geer, L. Haimberger, S. Healy, H. Hersbach, E. Hólm, L. Isaksen, P. Kållberg, M. Köhler, M. Matricardi, A. P. McNally, B. M. Monge-Sanz, J.-J. Morcrette, B.-K. Park, C. Peubey, P. de Rosnay, C. Tavolato, J.-N. Thépaut, and F. Vitart (2011), The ERA-Interim reanalysis: configuration and performance of the data assimilation system, *Quarterly Journal of the Royal Meteorological Society*, *137*(656), 553–597, doi:10.1002/qj.828.

Fridlind, A. M., A. S. Ackerman, J. P. Chaboureau, J. Fan, W. W. Grabowski, A. A. Hill, T. R. Jones, M. M. Khaiyer, G. Liu, P. Minnis, H. Morrison, L. Nguyen, S. Park, J. C. Petch, J. P. Pinty, C. Schumacher, B. J. Shipway, A. C. Varble, X. Wu, S. Xie, and M. Zhang (2012), A comparison of TWP-ICE observational data with cloud-resolving model results, *Journal of Geophysical Research*, *117*(D5), doi:10.1029/2011jd016595.

Gjorgjievska, S., and D. J. Raymond (2014), Interaction between dynamics and thermodynamics during tropical cyclogenesis, *Atmos. Chem. Phys.*, *14*, 3065–3082, doi:10.5194/acp-14-3065-2014.

Herman, M. J., and D. J. Raymond (2014), WTG cloud modeling with spectral decomposition of heating, *J. Adv. Model. Earth Syst.*, *06*, doi:10.1002/2014MS000359.

873 Inoue, K., and L. Back (2015a), Gross moist stability assessment during TOGA
874 COARE: Various interpretations of gross moist stability, *submitted*.

875 Inoue, K., and L. Back (2015b), Column-integrated moist static energy budget analysis
876 on various time scales during TOGA-COARE, *Journal of the Atmospheric Sciences*,
877 *72*(5), 1856–1871, doi:10.1175/JAS-D-14-0249.1.

878 Johnson, R., P. Ciesielski, J. J. Ruppert, and M. Katsumata (2015), Sounding-based
879 thermodynamic budgets for DYNAMO, *Journal of the Atmospheric Sciences*, *in press*,
880 doi:10.1175/JAS-D-14-0202.1.

881 Johnson, R. H., and P. E. Ciesielski (2013), Structure and properties of Madden-Julian
882 oscillations deduced from DYNAMO sounding arrays, *Journal of the Atmospheric*
883 *Sciences*, *70*(10), 3157–3179, doi:10.1175/jas-d-13-065.1.

884 Kim, D., P. Xavier, E. Maloney, M. Wheeler, D. Waliser, K. Sperber, H. Hendon,
885 C. Zhang, R. Neale, Y.-T. Hwang, and H. Liu (2014), Process-oriented MJO simu-
886 lation diagnostic: Moisture sensitivity of simulated convection, *Journal of Climate*,
887 *27*(14), 5379–5395, doi:10.1175/jcli-d-13-00497.1.

888 Kuang, Z. (2008), Modeling the interaction between cumulus convection and linear
889 gravity waves using a limited-domain cloud system-resolving model, *J. Atmos. Sci.*,
890 *65*, 576–591.

891 Madden, R. A., and P. R. Julian (1972), Description of global-scale circulation cells
892 in the tropics with a 40-50 day period, *Journal of the Atmospheric Sciences*, *29*,
893 1109–1123.

894 Masunaga, H. (2012), Short-term versus climatological relationship between precipita-
895 tion and tropospheric humidity, *J. Climate*, *25*, 7983–7990, doi:10.1175/JCLI-D-12-

896 00037.1.

897 Neelin, J. D., and I. M. Held (1987), Modeling tropical convergence based on the moist
898 static energy budget, *Mon. Weat. Rev.*, *115*, 3–12.

899 Peters, O., and J. D. Neelin (2006), Critical phenomena in atmospheric precipitation,
900 *Nat. Phys.*, *2*, 393–396, doi:10.1038/nphys314.

901 Raymond, D. J. (2001), A new model of the madden-julian oscillation, *Journal of the*
902 *Atmospheric Sciences*, *58*(18), 2807–2819.

903 Raymond, D. J. (2013), Sources and sinks of entropy in the atmosphere, *Journal of*
904 *Advances in Modeling Earth Systems*, *5*(4), 755–763, doi:10.1002/jame.20050.

905 Raymond, D. J., and S. L. Sessions (2007), Evolution of convection during tropical
906 cyclogenesis, *Geophys. Res. Lett.*, *34*, L06,811, doi:10.1029/2006GL028607.

907 Raymond, D. J., and X. Zeng (2005), Modelling tropical atmospheric convection in
908 the context of the weak temperature gradient approximation, *Quart. J. Roy. Meteor.*
909 *Soc.*, *131*, 1301–1320.

910 Raymond, D. J., S. K. Esbensen, C. Paulson, M. Gregg, C. S. Bretherton, W. A.
911 Petersen, R. Cifelli, L. K. Shay, C. Ohlmann, and P. Zuidema (2004), EPIC2001 and
912 the coupled ocean-atmosphere system of the tropical east Pacific, *Bull. Amer. Meteor.*
913 *Soc.*, *85*, 1341–1354.

914 Raymond, D. J., S. L. Sessions, and Z. Fuchs (2007), A theory for the spinup of tropical
915 depressions, *Q. J. Roy. Meteor. Soc.*, *133*, 1743–1754.

916 Raymond, D. J., S. L. Sessions, A. H. Sobel, and Željka Fuchs (2009), The mechanics of
917 gross moist stability, *J. Adv. Model. Earth Syst.*, *1*, 9, doi:10.3894/JAMES.2009.1.9.

Raymond, D. J., S. L. Sessions, and C. L. Carrillo (2011), Thermodynamics of tropical cyclogenesis in the northwest Pacific, *J. Geophys. Res.*, *116*, D18,101, doi: 10.1029:2011JD015624.

Raymond, D. J., S. Gjorgjievska, S. L. Sessions, and v. Fuchs (2014), Tropical cyclogenesis and mid-level vorticity, *Australian Meteorological and Oceanographic Journal*, *64*, 11–25.

Raymond, D. J., v. Fuchs, S. Gjorgjievska, and S. L. Sessions (2015), Balanced dynamics and thermodynamic constraints in the tropical troposphere, *Submitted to J. Adv. Model. Earth Syst.*, *64*.

Romps, D. M. (2012a), Weak pressure gradient approximation and its analytical solutions, *Journal of the Atmospheric Sciences*, *69*(9), 2835–2845, doi:10.1175/jas-d-11-0336.1.

Romps, D. M. (2012b), Numerical tests of the weak pressure gradient approximation, *Journal of the Atmospheric Sciences*, *69*(9), 2846–2856, doi:10.1175/jas-d-11-0337.1.

Sessions, S. L., S. Sugaya, D. J. Raymond, and A. H. Sobel (2010), Multiple equilibria in a cloud resolving model using the weak temperature gradient approximation, *J. Geophys. Res.*, *115*, D12110, doi:10.1029/2009JD013376.

Sessions, S. L., M. J. Herman, and S. Sentic (2015), Convective response to changes in the thermodynamic environment in idealized weak temperature gradient simulations, *Journal of Advances in Modeling Earth Systems*.

Sherwood, S. C., R. Roca, T. M. Weckwerth, and N. G. Andronova (2010), Tropospheric water vapor, convection, and climate, *Reviews of Geophysics*, *48*(2), doi: 10.1029/2009rg000301.

941 Sobel, A., S. Wang, and D. Kim (2014), Moist static energy budget of the MJO
942 during DYNAMO, *Journal of the Atmospheric Sciences*, *71*(11), 4276–4291, doi:
943 10.1175/JAS-D-14-0052.1.

944 Sobel, A. H., and G. Bellon (2009), The effect of imposed drying on parameterized deep
945 convection, *J. Atmos. Sci.*, *66*, 2085–2096, doi:10.1175/2008JAS2926.1.

946 Sobel, A. H., and C. S. Bretherton (2000), Modeling tropical precipitation in a single
947 column, *J. Climate*, *13*, 4378–4392.

948 Wang, S., and A. H. Sobel (2011), Response of convection to relative sea surface tem-
949 perature: cloud-resolving simulations in two and three dimensions, *J. Geophys. Res.*,
950 *116*, D11,119, doi:10.1029/2010JD015347.

951 Wang, S., A. H. Sobel, and Z. Kuang (2013), Cloud-resolving simulation of TOGA-
952 COARE using parameterized large-scale dynamics, *Journal of Geophysical Research:*
953 *Atmospheres*, *118*(12), 6290–6301, doi:10.1002/jgrd.50510.

954 Wang, S., A. H. Sobel, F. Zhang, Y. Q. Sun, Y. Yue, and L. Zhou (2014), Re-
955 gional simulation of the october and november MJO events observed during the
956 CINDY/DYNAMO field campaign at gray zone resolution, *Journal of Climate*, p.
957 141028075241006, doi:10.1175/jcli-d-14-00294.1.

958 Woolnough, S. J., P. N. Blossey, K. M. Xu, P. Bechtold, J. P. Chaboureau, T. Hosomi,
959 S. F. Iacobellis, Y. Luo, J. C. Petch, R. Y. Wong, and S. Xie (2010), Modelling con-
960 vective processes during the suppressed phase of a Madden-Julian oscillation: Com-
961 paring single-column models with cloud-resolving models, *Quarterly Journal of the*
962 *Royal Meteorological Society*, pp. n/a–n/a, doi:10.1002/qj.568.

963 Zhang, C. (2013), Madden-Julian oscillation: Bridging weather and climate, *Bulletin*
964 *of the American Meteorological Society*, *94*(12), 1849–1870, doi:10.1175/bams-d-12-
965 00026.1.

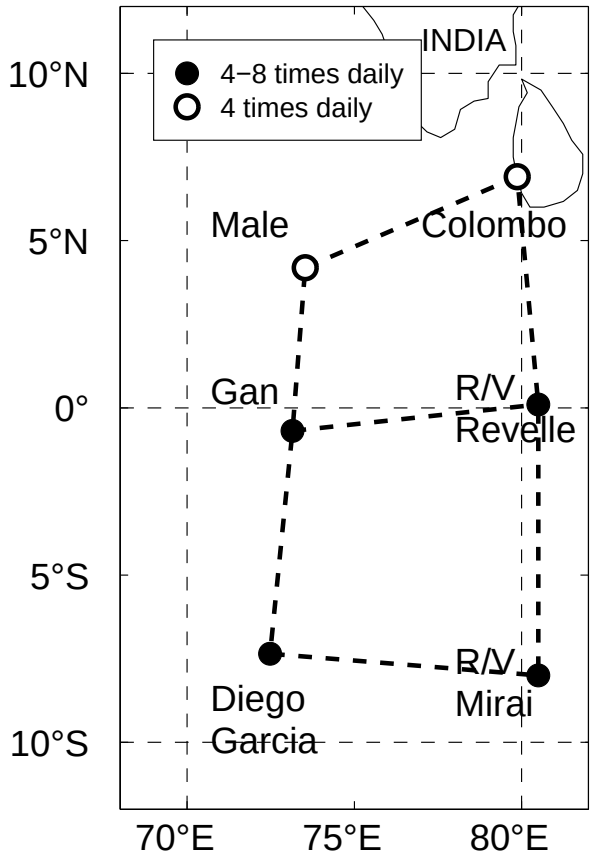

Figure 1. Station positions in the Dynamics of the Madden-Julian Oscillation (DYNAMO) campaign array.

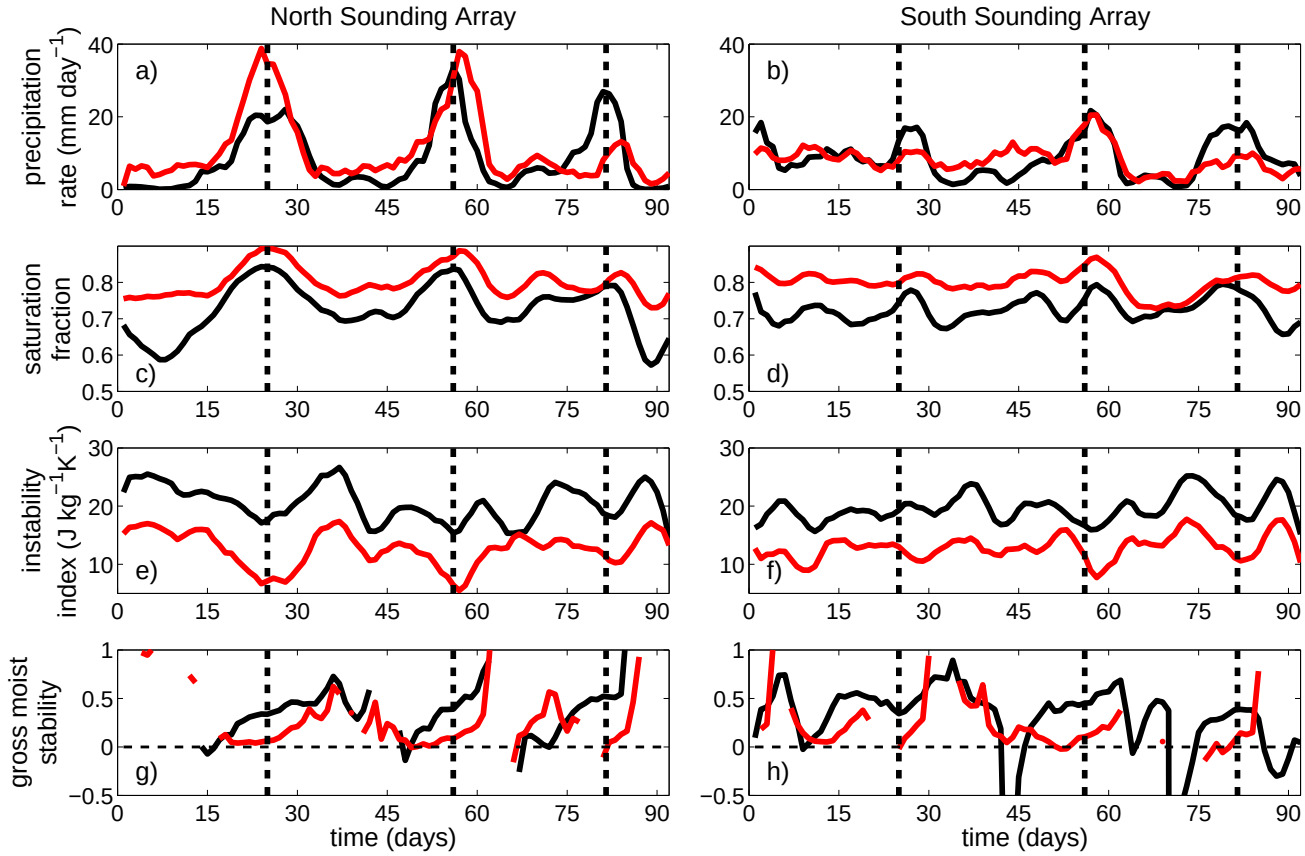

Figure 2. Smoothed (five day moving average) time series of precipitation rate (a–b), saturation fraction (c–d), instability index (e–f), and gross moist stability (GMS, g–h), for observations (black), and weak temperature gradient simulations (red). The North Sounding Array (NSA) are on the left (panels a, c, e, and g), and the South Sounding Array (SSA) are on the right (panels b, d, f, and h). Vertical dashed lines are rough guidelines aligned with observed precipitation maxima in the NSA. For comparison, NSA guidelines are plotted on the SSA panels (b,d,f, and h).

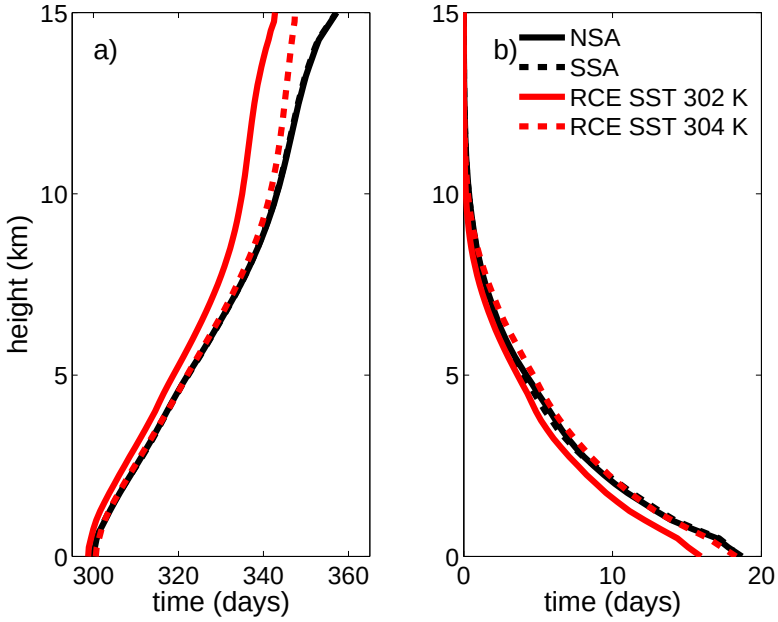

Figure 3. a) Potential temperature, and b) water vapor mixing ratio, for the model radiative-convective equilibrium (RCE, red), and observations: North Sounding Array (NSA, solid black) and South Sounding Array (SSA, dashed black). Note that the NSA and the SSA curves overlap. The RCE mean profiles corresponding to mean observed SSTs are cooler and dryer than the observed mean.

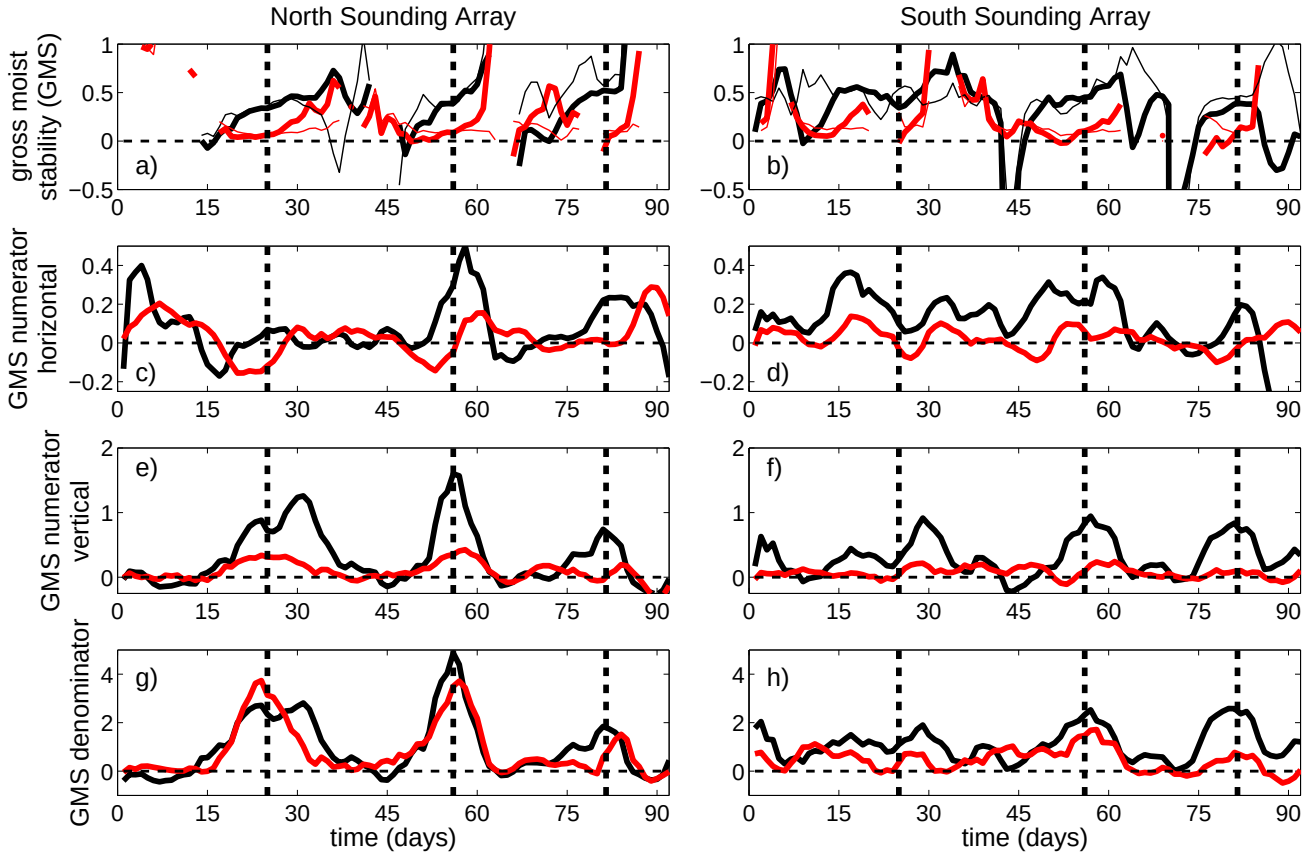

Figure 4. Smoothed (five day moving average) time series of the gross moist stability (GMS, panels a–b) and characteristic GMS(defined in equation 19, panels a–b), horizontal (c–d) and vertical (e–f) components of the GMS numerator, and the GMS denominator (g–h), for observations (black), and spectral weak temperature gradient simulations (red); for the North Sounding Array (NSA, panels a, c, e, and g), and the South Sounding Array (SSA, panels b, d, f, and h). Vertical dashed lines are rough guidelines aligned with observed precipitation maxima in the NSA. For comparison, NSA guidelines are plotted on the SSA panels (b, d, f, and h).

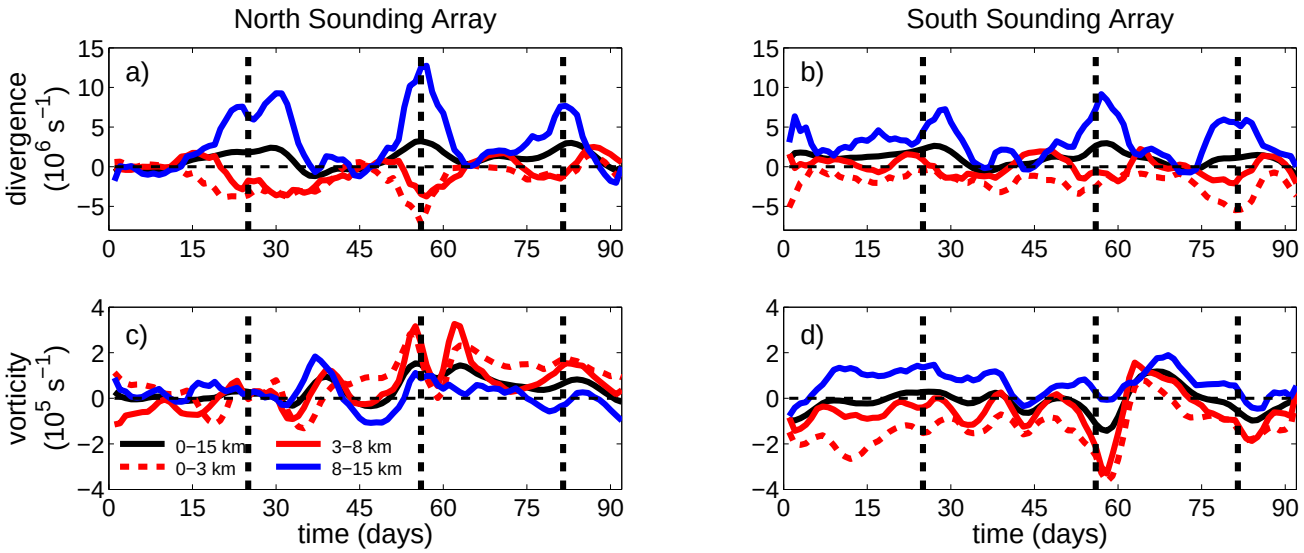

Figure 5. Observed time series of vorticity (a–b) and divergence (c–d) for the North Sounding Array (NSA, panels a and c), and the South Sounding Array (SSA, panels b and d). Time series were smoothed with with a five day moving average, and and averaged vertically in 0–15 km (solid black), 0–3 (dashed red), 3–8 km (solid red), and 8-15 km (solid blue) layers. Vertical dashed lines are rough guidelines aligned with observed precipitation maxima in the NSA. For comparison, NSA guidelines are plotted on the SSA panels (b, and d).

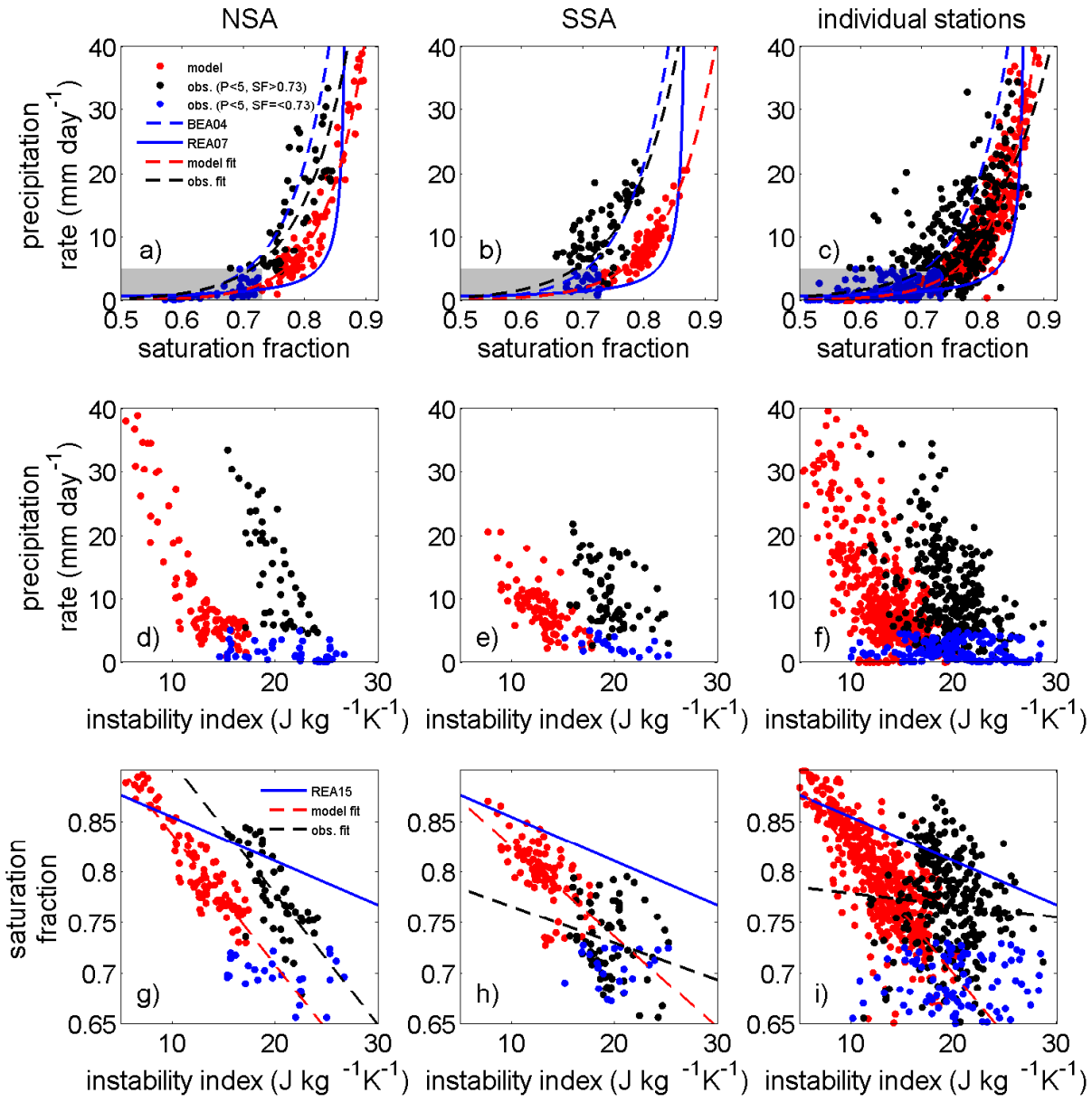

Figure 6. Relationships between precipitation rate and saturation fraction (top panels, a–c), precipitation rate and instability index (middle panels, d–f), and saturation fraction and instability index (bottom panels, g–i), for the North Sounding array (NSA, left panels, a, d, and g), South Sounding Array (SSA, middle panels, b, e, and f), and single station simulations (SS composite, right panels, c, f, and i).

Figure 6. (continued)

Observations are shaded blue for precipitation rates and saturation fractions smaller than 5 mm day^{-1} and 0.73, respectively, and black for the rest of the observed data, while the model is shaded in red. Precipitation rate–saturation fraction relationships from previous work are overlaid for comparison in the top row–dashed blue for *Bretherton et al.* [2004], and solid blue for *Raymond et al.* [2007]–while exponential fits for the DYNAMO observations and the model are the dashed black and red lines, respectively. The saturation fraction–instability index relationship from *Raymond et al.* [2015] has been overlaid for comparison in the bottom row–while linear relationship fits for the DYNAMO observations and the model are the dashed black and red lines, respectively. See table 2 for details about the fits.

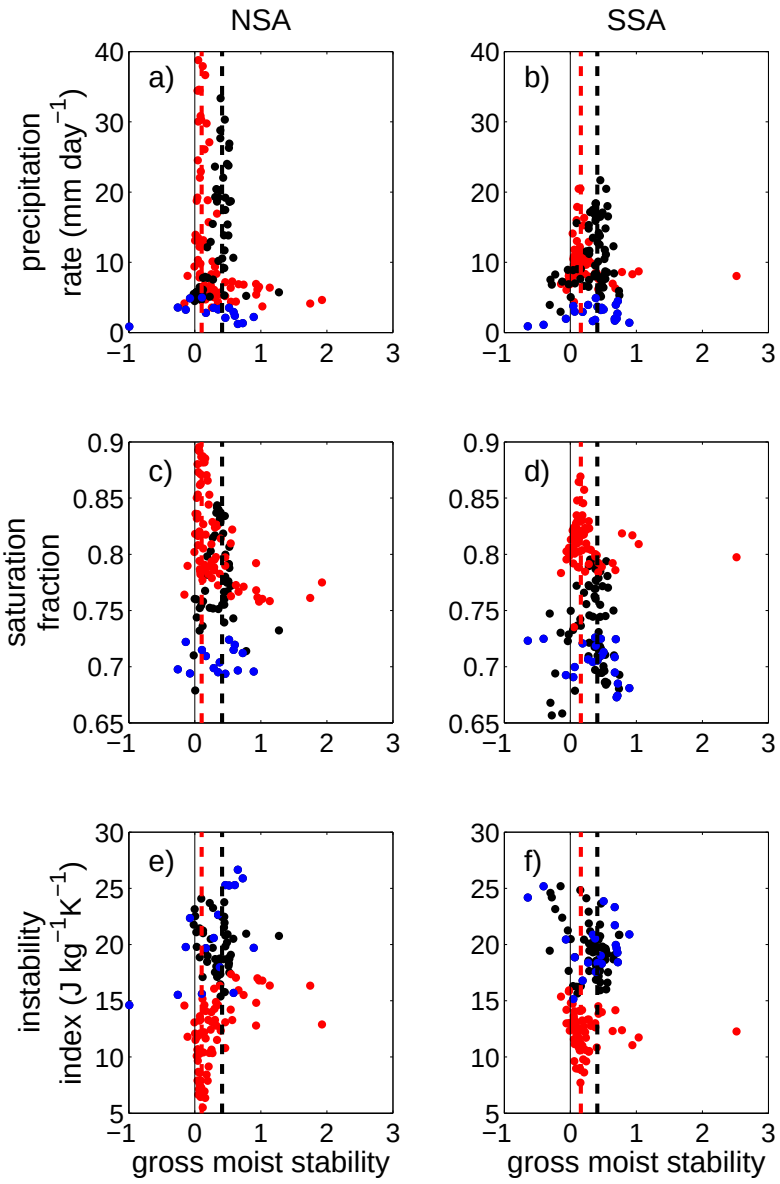

Figure 7. Relationships between the precipitation rate and the gross moist stability (GMS, top panels, a–b), saturation fraction and GMS (middle panels, c–d), and instability index and GMS (bottom panels, e–f), for the North Sounding array (NSA, left panels, a, c, and e), South Sounding Array (SSA, middle panels, b, d, and f). Observations are shaded blue for precipitation rates an saturation fractions smaller than 5 mm day^{-1} and 0.73, respectively, black for the rest of the observed data, while the model is shaded red. Vertical dashed lines represent the characteristic GMS value defined as the GMS at peak precipitation rates; black for observations (NSA 0.41, SSA 0.41), and red for the model (NSA 0.10, SSA 0.16).

Table 1. Characteristic gross moist stability* (GMS).

Characteristic GMS (Γ_C):	Γ'_{max}	$\tilde{\Gamma}'$	$\tilde{\Gamma}$	Γ_0
NSA Observations	0.412	0.428	0.395	0.372
NSA SWTG	0.103	0.065	0.098	0.137
SSA Observations	0.409	0.455	0.398	0.378
SSA SWTG	0.160	0.054	0.138	0.169

* Characteristic GMS calculated by all four methods listed by *Inoue and Back* [2015a, see text for definitions]; values for the North (NSA) and South (SSA) Sounding Arrays, for the observations, and spectral weak temperature gradient (SWTG) simulations.

Table 2. Diagnostic relationship fits*.

	Precipitation rate–saturation fraction $P(S) = \exp(b * (S - S_D))$		**Saturation fraction–instability index** $S(II) = c * II + d$	
	b	S_D	c (kg K J^{-1})	d
Bretherton et al. (2004)	15.6	0.603	/	/
Raymond et al. (2015)	/	/	-0.0433	0.897
NSA	13.39 ± 1.96	0.59 ± 0.03	-0.013 ± 0.004	1.04 ± 0.07
	16.36 ± 1.01	*0.67 ± 0.01*	*-0.013 ± 0.01*	*0.97 ± 0.02*
SSA	12.47 ± 2.69	0.56 ± 0.04	-0.0036 ± 0.0038	0.80 ± 0.07
	14.10 ± 1.31	*0.65 ± 0.02*	*-0.0089 ± 0.0023*	*0.91 ± 0.03*
Single station simulations	10.4 ± 1.04	0.55 ± 0.02	-0.00118 ± 0.0021	0.79 ± 0.04
	16.11 ± 0.62	*0.66 ± 0.01*	*-0.012 ± 0.001*	*0.94 ± 0.02*

* The precipitation rate–saturation fraction, and saturation fraction–instability index relationship fits, for the North Sounding Array (NSA), the South Sounding Array (SSA), and individual station simulations, compared to the relationships from previous work [*Bretherton et al.*, 2004; *Raymond et al.*, 2015].

Table 3. Modeled and observed statistics*.

	N (days)	Precipitation rate (mm day^{-1})	r	Saturation fraction (100%)	r	Instability Index (J kg^{-1} K^{-1})	r
NSA	92	8.4 ± 12.2 *11.1 ± 12.4*	**0.52**	0.73± 0.08 *0.80 ± 0.05*	**0.80**	20.6 ± 4.0 *12.7 ± 3.9*	**0.62**
SSA	92	8.7 ± 8.5 *8.4 ± 7.3*	**0.38**	0.72 ± 0.05 *0.80 ± 0.04*	**0.51**	19.7 ± 3.4 *12.9 ± 3.3*	**0.65**
Male	75	5.6 ± 9.9 *18.6 ± 19.1*	**0.59**	0.70 ± 0.11 *0.81 ± 0.07*	**0.86**	21.5 ± 6.2 *12.2 ± 5.0*	**0.60**
Colombo	71	6.6 ± 7.3 *9.2 ± 13.9*	**0.36**	0.72 ± 0.12 *0.74 ± 0.11*	**0.66**	20.0 ± 5.4 *12.6 ± 4.4*	**0.46**
Gan	92	7.5 ± 11.2 *9.1 ± 9.8*	**0.58**	0.75 ± 0.08 *0.79 ± 0.05*	**0.72**	19.7 ± 4.7 *13.1 ± 4.2*	**0.57**
R/V Revelle	61	10.5 ± 14.5 *15.9 ± 16.9*	0.30	0.77 ± 0.07 *0.81 ± 0.05*	0.07	19.9 ± 3.8 *16.6 ± 4.0*	0.01
Diego Garcia	92	9.1 ± 11.8 *8.1 ± 9.5*	**0.54**	0.73 ± 0.09 *0.78 ± 0.05*	**0.65**	20.8 ± 5.4 *13.0 ± 4.9*	**0.78**
R/V Mirai	61	6.2 ± 13.4 *15.6 ± 18.9*	0.28	0.65 ± 0.12 *0.80 ± 0.07*	-0.03	15.5 ± 4.9 *13.0 ± 5.1*	0.02

* Mean and standard deviation (observations roman, modeled italic), and lag zero correlation coefficients, r, between observed and modeled precipitation rate, saturation fraction, and instability index, for the DYNAMO North (NSA) and South (SSA) Sounding Arrays, and individual stations. N is the number of daily averages in time series (sample size). Correlation coefficients significant at the 98% level are in bold.

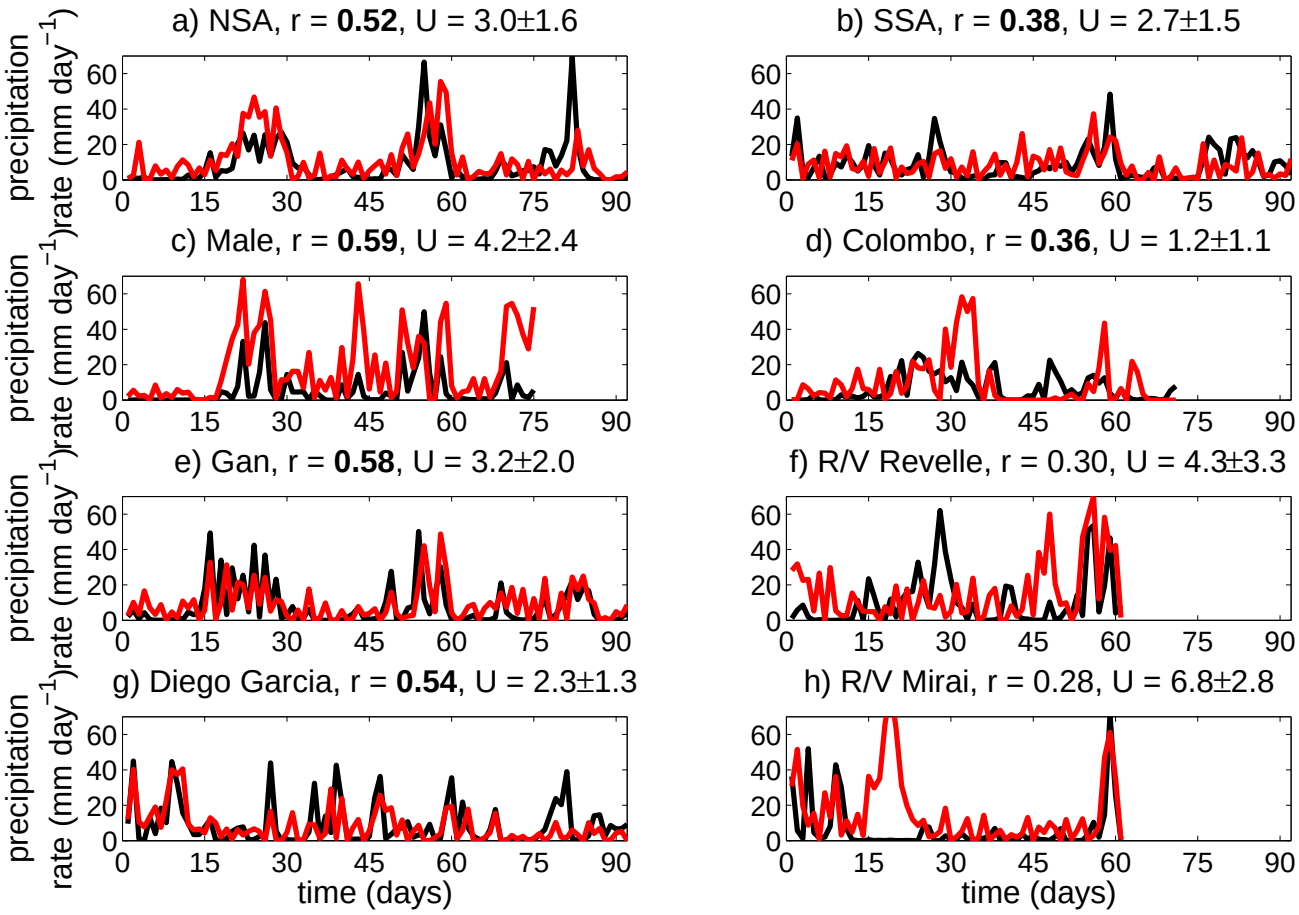

Figure 8. Observed (black) and modeled (red) daily precipitation rate time series for the north sounding array (NSA, panel a), south sounding array (SSA, panel b), and individual stations (panels c–h) from the Dynamics of the Madden-Julian Oscillation (DYNAMO) campaign. Correlation coefficients (r) between the observations and the model significant to 98% are in bold. The mean and the standard deviation of surface wind speeds is also given, for comparison.

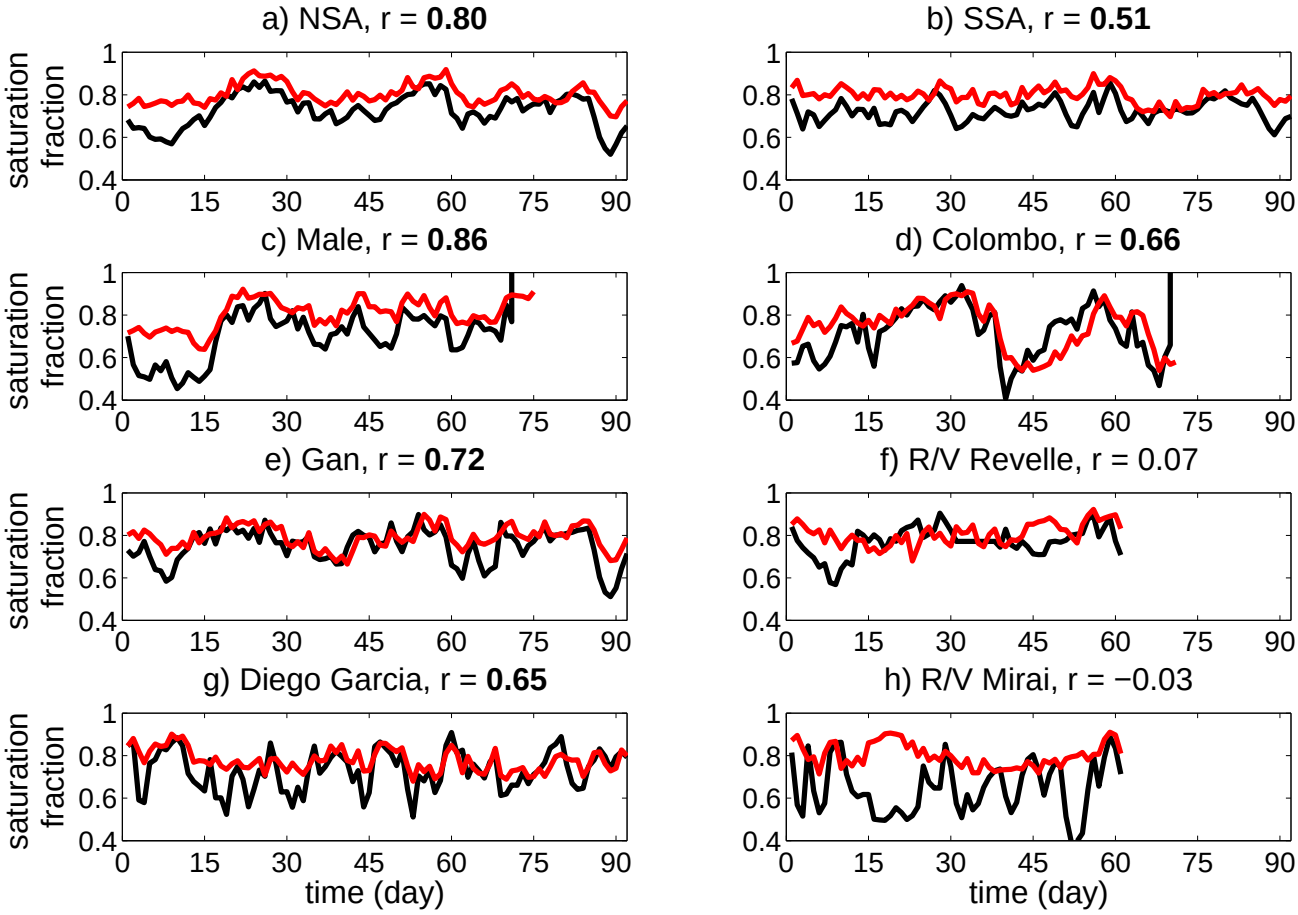

Figure 9. Same as figure 8, but for the saturation fraction.

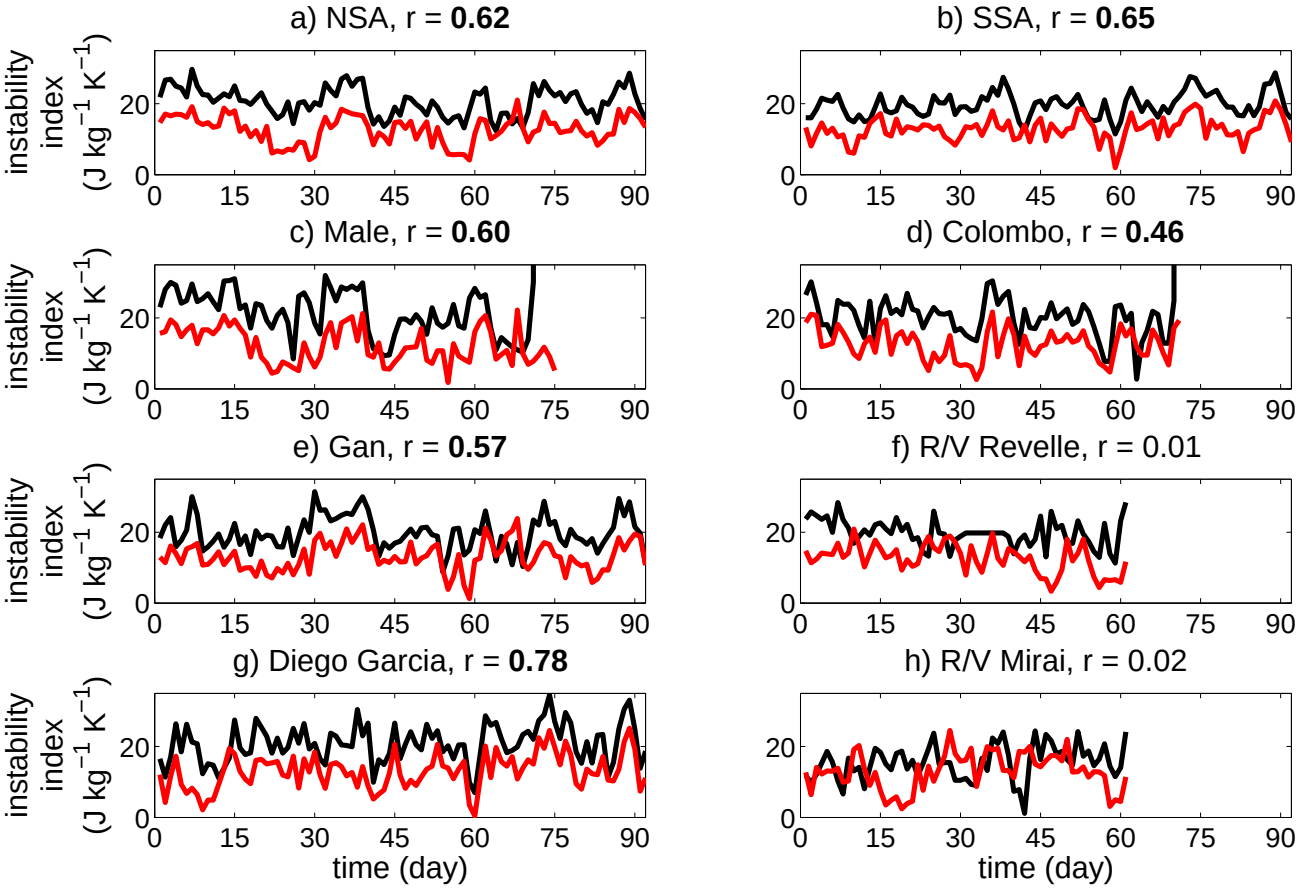

Figure 10. Same as figure 8, but for the instability index.